

Multiphase superconductivity in PdBi₂

Lewis Powell¹, Wenjun Kuang¹, Gabriel Hawkins-Pottier¹, Rashid Jalil¹, John Birkbeck¹, Ziyi Jiang¹, Minsoo Kim¹, Yichao Zou³, Sofiia Komrakova¹, Sarah Haigh³, Ivan Timokhin¹, Geetha Balakrishnan⁴, Andre K. Geim^{1,2}, Niels Walet¹, Alessandro Principi¹, Irina V. Grigorieva^{1,2}

¹Department of Physics and Astronomy, University of Manchester, Manchester M13 9PL, UK.

²National Graphene Institute, University of Manchester, Manchester M13 9PL, UK.

³Department of Materials, University of Manchester, Manchester M13 9PL, UK.

⁴Department of Physics, University of Warwick, Coventry CV4 7AL, UK

Abstract

Unconventional superconductivity, where electron pairing does not involve electron-phonon interactions, is often attributed to magnetic correlations in a material. Well known examples include high- T_c cuprates and uranium-based heavy fermion superconductors. Less explored are unconventional superconductors with strong spin-orbit coupling, where interactions between spin-polarised electrons and external magnetic field can result in multiple superconducting phases and field-induced transitions between them, a rare phenomenon in the superconducting state. Here we report a magnetic-field driven phase transition in β -PdBi₂, a layered non-magnetic superconductor. Our tunnelling spectroscopy on thin PdBi₂ monocrystals incorporated in planar superconductor-insulator-normal metal junctions reveals a marked discontinuity in the superconducting properties with increasing in-plane field, which is consistent with a transition from conventional (*s*-wave) to nodal pairing. Our theoretical analysis suggests that this phase transition may arise from spin polarisation and spin-momentum locking caused by locally broken inversion symmetry, with *p*-wave pairing becoming energetically favourable in high fields. Our findings also reconcile earlier predictions of unconventional multigap superconductivity in β -PdBi₂ with previous experiments where only a single *s*-wave gap could be detected.

Superconductivity in materials with spin-dependent correlations, either ferro- or antiferromagnetic, is often found to be unconventional¹⁻⁷. Here Cooper pairs are bound together not by the conventional electron-phonon interaction (*s*-wave pairing) but by other mechanisms, typically related to these materials' intrinsic magnetism. Furthermore, coupling between an external magnetic field and spin-polarised electrons can lead to a multiplicity of superconducting phases that exist in different regions of the temperature-magnetic field phase diagram¹⁻⁴. Such multiphase superconductivity is found in some heavy-fermion superconductors^{3,5-8}, as well as in liquid He-3^{1,9}. Complex phase diagrams and unconventional superconductivity are also predicted in materials with strong spin-orbit coupling (SOC) due to spin-momentum locking, but the nature of superconductivity in this case is much less explored, especially experimentally. Recent findings include topologically protected surface superconductivity¹⁰, superconducting diode effect¹¹ and critical fields greatly exceeding the paramagnetic Pauli limit¹²⁻¹⁶. An emergence of phase transitions is another enticing possibility, e.g., an external magnetic field can distort the spin-locked Fermi surfaces, changing the energy balance between superconducting phases with different pairing symmetries¹⁷. However, the even-parity (spin-singlet) and odd-parity (spin-triplet) superconducting order parameters in such materials are typically mixed^{18,19} and phase transitions in the superconducting state are rare, with recently reported heavy fermion CeRh₂As₂²⁰⁻²² and Li-intercalated

bilayer MoS_2 ²³ the only known examples. In addition, the complexity of competing interactions allows alternative interpretations of the experimentally observed phase diagrams²¹ and further studies on different experimental systems are needed to unravel the mechanisms underpinning the effect of magnetic field.

Here we report a magnetic-field driven phase transition within the superconducting state of the layered tetragonal superconductor $\beta\text{-PdBi}_2$. Its basic superconducting properties were described in the literature already in the 1950s^{24,25}. More recently, theory identified it as a candidate topological superconductor, where multiple superconducting gaps with different symmetries are expected to open on different Fermi surfaces²⁶⁻²⁹. Band structure calculations²⁶, angle-resolved photoemission spectroscopy (ARPES)^{27,30} and quasiparticle interference imaging (QPI)²⁸ found spin textures both in the surface and bulk electronic bands. Yet, only single-gap s -wave superconductivity could be detected so far in a range of different experiments³¹⁻³³, with only one recent neutron scattering study indicating a possibility of two gaps of different magnitude and/or momentum-dependent gap anisotropy³⁴. In our work we used tunnelling spectroscopy on PdBi_2 -hBN-few-layer-graphene heterostructures and resistance measurements on exfoliated crystals, and found evidence of a magnetic-field driven phase transition: While at low fields B , both in-plane and out-of-plane, $\beta\text{-PdBi}_2$ behaves as a conventional s -wave superconductor, at in-plane $B \sim 0.1\text{-}0.2$ T we observed a transition to a new superconducting state with characteristics of unconventional pairing and a nodal gap. This is seen as a sharp change in the characteristics of the tunnelling spectra above and below a transition field B^* (zero-bias conductance, extracted gap value, pair-breaking strength), as well as a kink in the phase diagram $B_{c2}(T)$ for the in-plane field.

Results

Importantly for the present study, we were able to grow high-quality single crystals of the tetragonal $\beta\text{-PdBi}_2$, see X-ray diffraction in Supplementary Fig. 1b. The high crystal quality is further confirmed by the exceptionally low hysteresis in the DC magnetization, $M(B)$, and the sharpness of the superconducting transition, Fig. 1e and Supplementary Fig. 1a. The superconducting coherence length ξ and magnetic field penetration depth λ for our PdBi_2 were determined from the critical fields B_{c1} and B_{c2} obtained from magnetization measurements (Methods), yielding $\xi_{\text{ab}}(0) \approx 22$ nm (in-plane coherence length), $\xi_c(0) \approx 17$ nm (out-of-plane) and $\lambda(0) \approx 240$ nm. The in-plane coherence length is only slightly shorter than the low-temperature mean free path $l \approx 25$ nm determined from magnetoresistance measurements on relatively thick (~ 1 μm thick) crystals from the same batch.

To measure the superconducting gap Δ , we have fabricated superconductor-insulator-normal metal (SIN) tunnel junctions, where thin slabs of PdBi_2 mechanically exfoliated from a bulk crystal (such as shown in Supplementary Fig. 1b) served as the superconducting electrode. Few-layer graphene (FLG) and 2-3 layer thick hBN were used as the normal electrode (N) and the insulating barrier (I), respectively. Figure 1b,c shows an optical image and a schematic of a typical device (see Methods for fabrication details). Cross-sectional transmission electron microscopy on one of the used devices (Methods and Fig. 1d) verified that the fabrication process did not induce any phase transformations, nor introduced defects. The design allowed us to measure both the tunnelling conductance and the resistance in Hall bar geometry on the same device. Five devices were studied, containing PdBi_2 crystals with thicknesses between 50 and 140 nm. They all showed the same qualitative behaviour but quantitative characteristics (critical temperature T_c , upper critical field B_{c2}) were found to depend on the thickness d and were different from those for bulk crystals (10-100 μm thick). While it would be interesting to study even thinner crystals, unfortunately we found it impossible to exfoliate crystals with $d < 50$ nm and lateral

dimensions sufficient for device fabrication (see Methods for details). Typical examples described in detail below are for devices with $d = 80\text{nm}$ (device A) and $d = 50\text{nm}$ (device B).

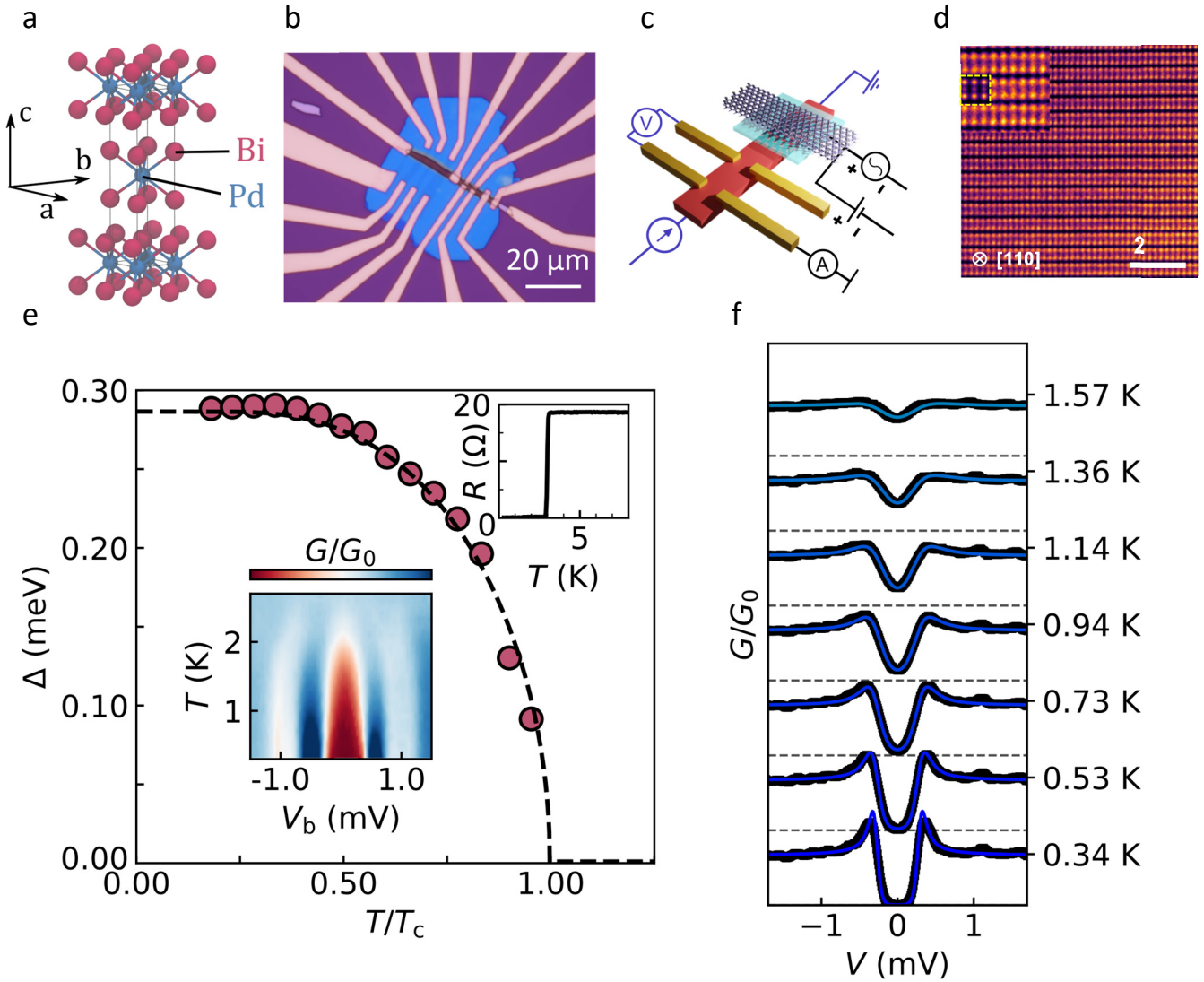


Figure 1 | Device design and tunnelling characteristics of $\beta\text{-PdBi}_2$. **a**, Crystal structure of $\beta\text{-PdBi}_2$. Bismuth atoms within each Bi-Pd-Bi layer are arranged tetragonally around Pd to form a square Bi bilayer. Neighbouring layers are staggered in an AB configuration. **b**, Optical image of one of our devices. **c**, Schematic of a device combining a tunnelling conductance measurement scheme (black) and four-probe contact configuration for resistance measurements (blue). For tunnelling, few-layer graphene (ball and stick model) acts as the normal metal, PdBi_2 is the superconducting electrode (red) and 2-3 layer insulating hBN is used as a tunnel barrier (cyan). The entire structure is encapsulated in 100 nm hBN, not shown here. **d**, Atomic-resolution cross-sectional STEM image of a thin slice lifted from a device after completing the tunnelling measurements (Methods). The inset shows a zoomed-in section of the main image overlapped with the simulated HAADF image (the latter outlined by the yellow dashed line). **e**, *Main panel*: Temperature-dependent superconducting gap, $\Delta(T)$, extracted from fitting individual tunnelling spectra for device B (symbols). Dashed line is a fit to weak-coupling BCS theory. *Insets*: Superconducting transition in $R(T)$ (top) and a zero-field tunnelling conductance map (bottom). **f**, Zero-field tunnelling spectra at different T , see labels. The spectra (black symbols) are accurately described by the standard Dynes model (solid blue line). Data for device B.

The differential tunneling conductance $G(V_b) = dI(V_b)/dV$ was measured by applying a small AC excitation $dV \sim 50 \mu\text{V}$ superimposed on a DC bias voltage V_b , and detecting the AC current dI between the top (FLG) and bottom (PdBi₂) electrodes. At low T and zero B we observed spectra typical for conventional SIN tunnel junctions³⁵, with a full gap seen as zero conductance for $V_b < 0.2 \text{ mV}$, and sharp conductance peaks just above the gap (Fig. 1f). To quantify Δ as a function of T , we fitted the measured tunneling conductance $G_{\text{NS}}(V_b)$ using the standard expression³⁵

$$G_{\text{NS}} = \frac{dI}{dV} = \frac{G_{\text{NN}}}{N_{\text{N}}(0)} \int_{-\infty}^{+\infty} N_{\text{S}}(E, \Gamma, \Delta) \frac{\partial f(E + eV_b, T)}{\partial(eV_b)} dE, \quad (1)$$

where G_{NN} corresponds to both electrodes being in the normal state, $N_{\text{N}}(0)$ and $N_{\text{S}}(E, \Gamma, \Delta)$ are the density of states (DoS) at the Fermi level for the superconducting electrode in the normal and superconducting state, respectively; $f(E + eV_b, T)$ the Fermi-Dirac distribution, E the quasiparticle energy and Γ the quasiparticle lifetime broadening parameter. The superconducting DoS is given by the Dynes formula³⁶

$$\frac{N_{\text{S}}(E, \Gamma, \Delta)}{N_{\text{N}}(0)} = \text{Re} \left[\frac{E - i\Gamma}{(E - i\Gamma)^2 - \Delta^2} \right]. \quad (2)$$

Figure 1e shows the conductance map and the order parameter $\Delta(T)$ extracted from individual spectra, such as shown in Fig. 1f. Here $\Delta(T)$ is well described by the universal formula for the BCS gap, $\Delta(T) = 1.76k_{\text{B}}T_{\text{c0}} \tanh(1.74\sqrt{T_{\text{c0}}/T - 1})$, indicating standard s -wave superconductivity at $B = 0$.

In contrast, the evolution of the tunnelling spectra with magnetic field is highly unusual. Firstly, there is a large anisotropy between the in-plane and out-of-plane B . This is seen qualitatively in the conductance maps of Fig. 2a,b: In perpendicular field, B^{\perp} , the gap – indicated approximately by the width of the low G/G_0 region (brown area of the maps) – decreases smoothly, and the evolution of the individual spectra is qualitatively similar to their evolution as a function of temperature (c.f. Fig. 1f and Supplementary Fig. 2a). However, in parallel field, B^{\parallel} (Fig. 2a) there are two distinct regions in the B dependence: below $\sim 0.2\text{T}$ the gap is rapidly suppressed until a pronounced ‘kink’ appears at $B^* \approx 0.2\text{T}$, after which it decreases slowly up to $B_{\text{c2}} \approx 1.6\text{T}$. Additionally, distinct responses above and below B^* are seen in individual spectra, not only in the spectral shape and zero-bias conductance (ZBC), where qualitative changes are clear in Fig. 2c, but also in the evolution of the parameters describing the spectra, the order parameter $\Delta(B)$ and the pair-breaking strength ζ (see below for a detailed discussion). In terms of the field sweep direction, with our experimental accuracy there was no discernible difference in the tunnelling spectra measured in an increasing/decreasing field.

The anisotropy is further evidenced in the phase diagram, Fig. 2d, which compares the T dependence of the in-plane and out-of-plane upper critical field, B_{c2} . In contrast to smooth linear increase of $B_{\text{c2}}^{\perp}(T)$, as is typical for thin films³⁵, $B_{\text{c2}}^{\parallel}(T)$ shows a clear kink and two distinct regions on the phase diagram. Here we used measurements of the resistance $R(T, B)$ on the same exfoliated PdBi₂ crystals in the Hall bar configuration (see schematic in Fig. 1c), taking the values of B at which the resistance is 90% of the normal-state value (just below the transition to the superconducting state) as B_{c2} . As the $R(B)$ curves for in-plane field were always sharp, varying this criterion had little effect on the extracted B_{c2} and did not change the two trends. We note that the sharpness of the resistance curves at all T (Fig. 2e) is consistent with the absence of vortices, as both B and Δ are essentially uniform over the crystal thickness $d \sim (2 - 3)\xi \ll \lambda$. For comparison, Supplementary Fig. 2b shows $R(T, B^{\perp})$ for the out-of-plane field, where the presence of vortices broadens the resistance curves, particularly at low T .

We first analyse the observed tunnelling conductance for in-plane B in light of the known evolution of the DoS for an s -wave superconductor. For a qualitative comparison, we modelled the tunnelling spectra using Maki’s solutions of the generalized Gorkov equation for a thin film in parallel field^{37–40}, i.e., such that both B and Δ are uniform across the film’s thickness. (Assuming that the coherence length ξ and

penetration depth λ in exfoliated PdBi_2 crystals are approximately the same as in our bulk samples, this condition is satisfied for all our devices having $d \lesssim 100$ nm.) As illustrated in Supplementary Fig. 3a, the modelled spectra have the following qualitative features: (i) a full gap of decreasing size persists up to B close to $\sim 0.7B_{c2}$, with ZBC remaining zero; (ii) only at $B > 0.7B_{c2}$ does superconductivity become gapless, with a rapid increase in ZBC; (iii) quasiparticle peaks are almost fully suppressed by a relatively low $B \sim 0.5B_{c2}$, while the spectra remain fully gapped. All these features have been reported in the literature for the tunnelling spectra of conventional superconductors (Sn, Sn-In^{38,39}) and they are also seen in our experiment in the low-field region, $B^{\parallel} \lesssim B^*$, see Fig. 2c and Supplementary Figs. 4 and 5a. In contrast, above B^* , the spectra become “V”-shaped and ZBC increases rapidly, indicating the presence of low-energy quasiparticle excitations inside the gap^{41,42}. The latter observation is particularly unusual as it indicates *gapless* superconductivity over a wide range of $B \ll B_{c2}$, in stark contrast to the conventional behaviour but consistent with nodal superconductivity^{41,42}. More subtle differences between the two regions of magnetic field are seen in the spectral peaks corresponding to quasiparticle excitations just above the gap: below B^* their height is rapidly suppressed by increasing B^{\parallel} , as expected for a conventional superconductor, but no further suppression is seen above B^* and they remain prominent up to $B \sim 0.5B_{c2}$ (Fig. 2c).

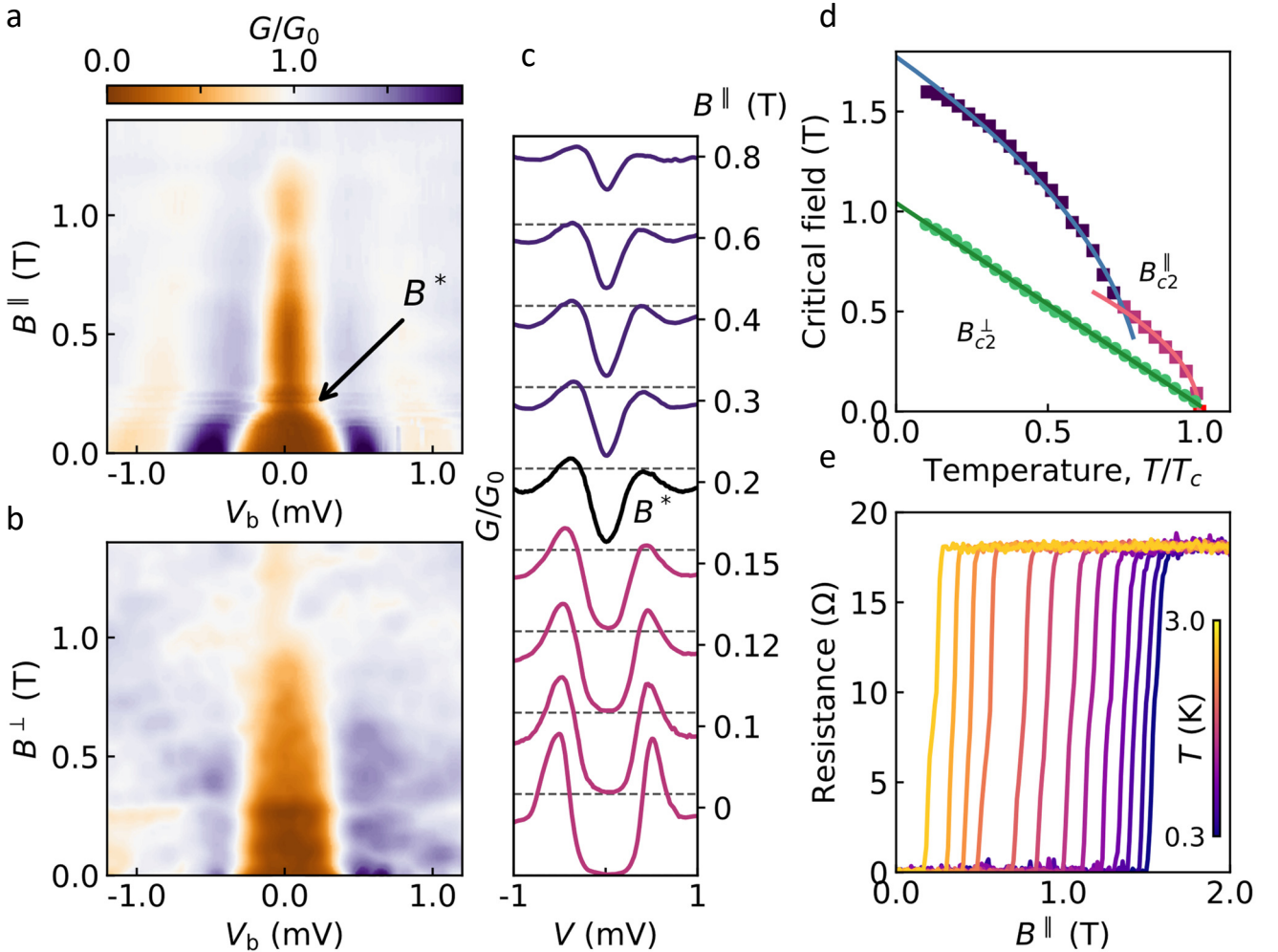


Figure 2 | Phase transition under in-plane magnetic field. **a,b**, Maps of the normalised tunnelling conductance for in-plane (a) and out-of-plane (b) magnetic fields. $T = 0.3$ K. G_0 corresponds to both electrodes being in the normal state. Brown areas correspond approximately to the spectral gap. Arrow in (a) indicates the transition field B^* (see text). **c**, Selected spectra from (a) emphasising the change in spectral shape at B^* . Values of B are shown as labels. Dashed horizontal lines correspond to $G/G_0 = 0$. **d**, Temperature-dependent upper critical fields for in-plane and out-of-plane B extracted from $R(B)$ measurements, such as shown in (e). Shown values of B_{c2} correspond to $R = 0.9R_N$, where R_N is the

normal state resistance. Green circles show B_{c2}^{\perp} , red squares B_{c2}^{\parallel} below the kink at 0.5T, and blue squares B_{c2}^{\parallel} above 0.5T. Solid lines are fits to eqs. (4) and (5), see text. **e**, Resistance vs in-plane magnetic field at different T . Data for device A.

More quantitatively, Maki theory^{37,43} allows using tunnelling conductance to evaluate the two parameters that describe the effect of in-plane magnetic field on superconductivity: the order parameter $\Delta(B^{\parallel})$ and the depairing strength $\zeta(B^{\parallel})$ due to time-reversal-breaking perturbations that split Cooper pairs, see eqs. (9)-(12) in Methods. The theory is known to accurately describe $\Delta(B^{\parallel})$ and $\zeta(B^{\parallel})$ in conventional superconductors such as Sn^{38,39}. We emphasise that no further fitting parameters – beyond $\Delta(B^{\parallel})$ and $\zeta(B^{\parallel})$ – are needed to describe the tunnelling spectra for a material with a relatively low B_{c2} , such as PdBi₂ (Methods). In fact, the majority of the changes are due to the pair-breaking effect of the magnetic field (compare Supplementary Figs. 3b and 3c). Other quantities appearing in eqs. (9)-(12) are fixed: T is the experimental temperature (0.3K or 0.1 T_c) and the g-factor, known to be $g \approx 2$ for β -PdBi₂, fixes the Zeeman energy $\mu_B B$.

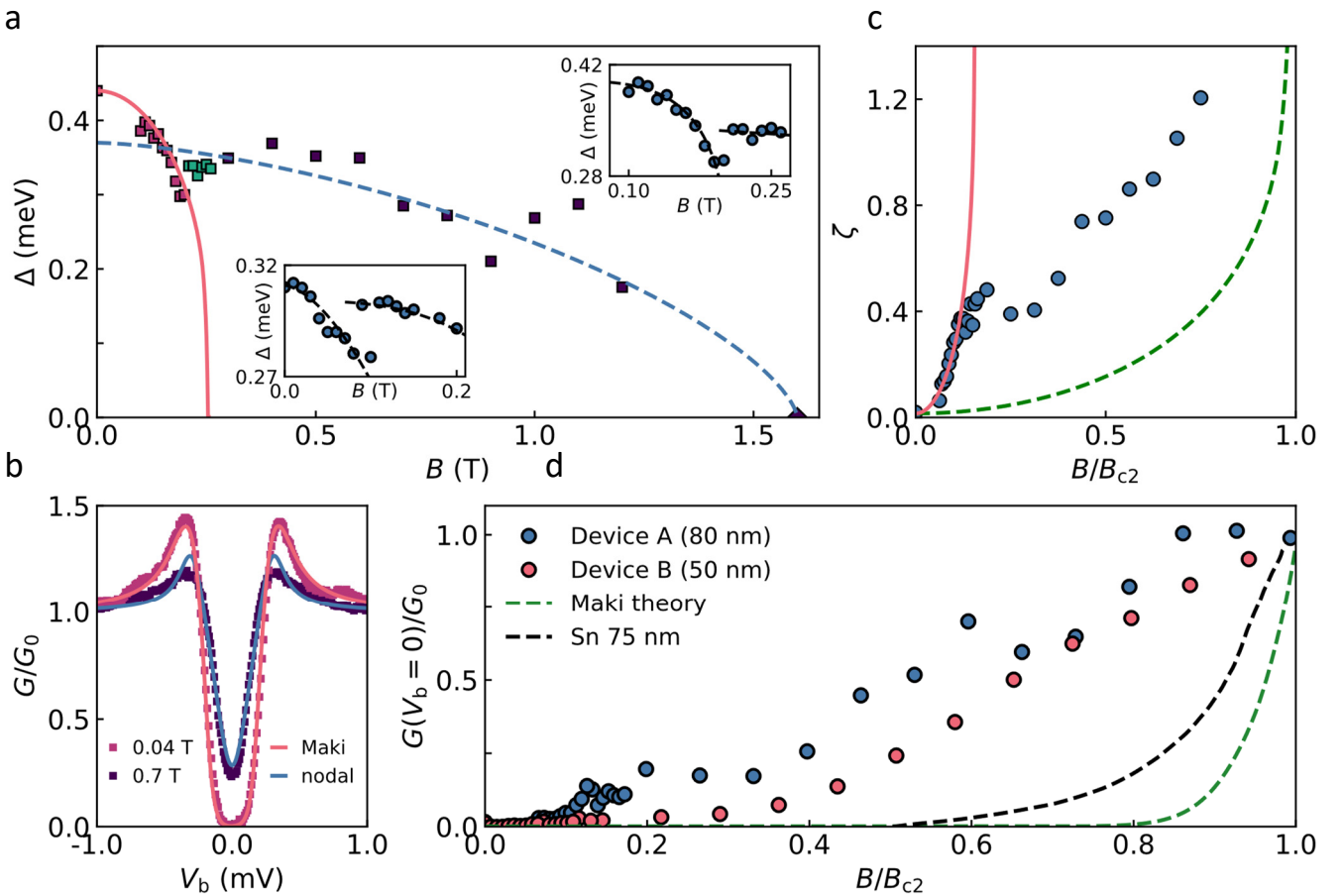


Figure 3 | Superconducting gap of PdBi₂ for in-plane magnetic field. **a**, *Main panel*: Superconducting order parameter Δ extracted from fits to individual spectra vs in-plane magnetic field B^{\parallel} . Data for device A ($d \approx 80$ nm), $T = 0.3$ K. Red squares correspond to $\Delta(B^{\parallel})$ extracted using the Maki theory and BCS DoS, dark-blue squares to nodal DoS (see text), and green squares are fits to the Maki theory in the intermediate region. Red solid line is a fit to eq. (10) yielding an apparent critical field for low- B s-wave superconductivity $B_c^{s\text{-wave}} \approx 0.25$ T. Dashed blue line is a guide to the eye. *Insets*: Detailed view of $\Delta(B^{\parallel})$ in the low- B region for device A (top inset) and device B (bottom inset). A pronounced kink in $\Delta(B^{\parallel})$ seen for both devices corresponds to suppression of the s-wave gap followed by the appearance of a new order parameter, as emphasised by the dashed lines (guides to the eye). **b**, Representative spectra at $B < B^*$ (red squares) and $B > B^*$ (dark-blue squares) revealing the change from conventional (s-wave) to nodal gap. Solid lines are fits to the two models, see legend. Details of fitting are explained in Methods. **c**, Evolution of the depairing strength parameter $\zeta(B^{\parallel})$ extracted from fitting of the experimental spectra

to the Maki theory (blue symbols). Below B^* , ζ follows the expected behaviour for an s -wave superconductor with a critical field $B_c^{s\text{-wave}} = 0.25$ T; this is shown by the red solid line calculated using eqs. (11)-(12) (Methods). Dashed green line shows $\zeta(B^{\parallel})$ calculated using the same equations for an s -wave superconductor with $B_{c2} = 1.6$ T (actual upper critical field for our PdBi₂). Attempting to apply the Maki theory above B^* (as detailed in Supplementary Fig. 5b) results in unphysically large values of ζ ; this is clear from comparison between the extracted ζ (blue symbols) and the theory prediction (dashed green line). **d**, Evolution of zero-bias conductance with B^{\parallel} for device A (blue) and device B (red). For comparison, dashed lines show corresponding results predicted by theory³⁷ (green) and experimental data for a conventional BCS superconductor (75nm Sn film) taken from ref. ³⁹ (black).

Fig. 3a-c and Supplementary Fig. 5a demonstrate that the theory provides a good fit to the low- B spectra for our PdBi₂, $\Delta(B^{\parallel} < B^*)$ and $\zeta(B^{\parallel} < B^*)$, which is further evidence that below B^* its superconductivity is underpinned by conventional s -wave pairing. In contrast, at $B^{\parallel} > B^*$ the fits to the Maki theory become poor and the fast-increasing ZBC cannot be described by any realistic value of the depairing strength ζ , see Fig. 3b and Supplementary Fig. 5b. Persistence of the quasiparticle peaks well beyond B^* is also contrary to the theory expectations (compare modelling in Supplementary Fig. 3a with experimental spectra in Fig. 2c and Supplementary Figs 4 & 5b).

As for the effect of the out-of-plane field, no kink in $G(V_b, B_{\perp})$ or other evidence of a field-induced phase transition could be seen in any of our devices (see Supplementary Fig. 2a for an example) and we therefore conclude that superconductivity in this case remains s -wave. We note however that the spectra in an out-of-plane field are not directly related to DoS and cannot be fitted by any simple model as vortices can contribute to the mid-gap conductance.

We now show that all the above field-induced changes in the superconducting characteristics of our PdBi₂ can be explained by a transition from conventional s -wave pairing to nodal superconductivity, with anisotropic p -wave pairing being the most likely candidate in the latter case. An excess ZBC and a Dirac-like sub-gap DoS are well-known characteristics of a superconducting gap vanishing at lines on the Fermi surface ^{41,42}. In our devices ZBC increases sharply (approximately linearly) as soon as B exceeds B^* , Fig. 3d. For a more quantitative relationship, we fitted the high-field spectra using DoS for a nodal p -wave order parameter $\Delta_{\hat{k}} = \Delta \cos \theta_k$, and including a ‘broadening’ parameter Γ due to pair-breaking effects (see Supplementary Note 2.1 for a derivation):

$$\frac{N_S(E, \Gamma, \Delta)}{N_N(0)} = \text{Re} \left[\frac{E + i\Gamma}{\Delta} \arcsin \left(\frac{\Delta}{E + i\Gamma} \right) \right]. \quad (3)$$

As shown in Fig. 3b and Supplementary Fig. 5b, the nodal DoS fits the spectra accurately at all $B > B^*$, whilst the fits with the Maki model are poor even if we allow the pair-breaking strength ζ to take on unrealistically high values (see Supplementary Fig. 5b for a detailed explanation). As below B^* the tunnelling spectra are accurately described by the Maki theory, we use eqs. (9)-(12) (Methods) to extract the order parameter $\Delta(B)$ at $B \leq B^*$ and for $B > B^*$ use eq. (3). The results are shown in Fig. 3a. Similar to the suppression of the superconducting gap seen qualitatively in the conductance map in Fig. 2a, at low B the order parameter is rapidly suppressed, tending towards an extrapolated critical field ≈ 0.25 T (red curve in Fig. 3a). At $B^* \approx 0.2$ T, Δ is seen to increase again, in agreement with the ‘kink’ seen in raw $G(V_b, B^{\parallel})$ in Fig. 2a, and at $B > 0.5$ T starts to decrease slowly towards $B_{c2} \approx 1.6$ T. The spectra in the transitional region between $B \sim 0.2$ and 0.4 T can be fitted equally well by eqs. (9)-(12) and eq. (3) (i.e., no preference to either the Maki or nodal model).

The sharp suppression of the conventional s -wave order parameter followed by a transition towards a larger Δ and a slow approach towards $\Delta = 0$ at B_{c2} is seen in all our devices, the only difference being

the exact value of B^* which generally decreases for thinner crystals (cf. $\Delta(B)$ for $d = 50$ and 80 nm in Fig. 3a). Together with the increase in ZBC, the changes in the spectral shape and the different evolution of the pair-breaking strength $\zeta(B)$ above and below B^* (Fig. 3b), this implies a transition from conventional s -wave pairing to a new, field-induced, phase characterized by unconventional nodal pairing.

The phase diagram in Fig. 2d - $B_{c2}^{\parallel}(T)$ and $B_{c2}^{\perp}(T)$ - provides a further insight into the effect of magnetic field on the superconductivity of β -PdBi₂. As shown in Fig. 2d, out-of-plane $B_{c2}^{\perp}(T)$ is accurately described by the 2D Ginzburg-Landau (GL) theory³⁵ at all B and T , indicating conventional behaviour:

$$B_{c2}^{\perp}(T) = \frac{\Phi_0}{2\pi\xi_{ab}(0)^2} \left(1 - \frac{T}{T_c}\right). \quad (4)$$

Here Φ_0 is the magnetic flux quantum and ξ_{ab} the in-plane coherence length. The fit yields $\xi_{ab}(0) = 18$ nm and $B_{c2}^{\perp}(0) \approx 1$ T, close to the extrapolated bulk values of about 20 nm and 0.8T. In contrast, and in agreement with our findings from tunnelling spectroscopy, $B_{c2}^{\parallel}(T)$ cannot be described by a single GL fit due to a kink at $B \sim 0.5$ T, which implies that the low- B superconducting phase is eclipsed by a different phase at higher B . Individually, both parts of the $B_{c2}^{\parallel}(T)$ curve can be described by the GL expression³⁵

$$B_{c2}^{\parallel}(T) = \frac{\sqrt{12}\Phi_0}{2\pi\xi_{ab}d} \sqrt{1 - \frac{T}{T_c}}, \quad (5)$$

with the low- B fit yielding $d = 63$ nm, close to the actual thickness of the PdBi₂ crystal, 80nm. While 0.5T is notably above B^* for this device, this is likely because the kink in $B_{c2}(T)$ is where the high-field superconductivity completely overtakes the s -wave phase, whereas the kink in $G(V_b)$ corresponds to its onset. Indeed the field corresponding to the kink in $B_{c2}(T)$ in Fig. 2d is close to B corresponding to the maximum for the nodal order parameter in Fig. 3a.

The above results, using different experimental probes, show that only a single s -wave gap is present in zero- and out-of-plane B , in agreement with previous studies^{28,31}. This suggests that any unconventional pairing in this case is either energetically unfavourable or obscured by a larger BCS gap, whereas a sufficiently strong in-plane B favours pairing in the unconventional channel. This was hinted at in a recent neutron scattering experiment³⁴ where an unusual T dependence of the superfluid density indicated unconventional pairing in B^{\parallel} but not in B^{\perp} .

Discussion

To explain the observed field-induced transition in the superconducting state, we have constructed a minimal tight-binding model (Methods and Supplementary Note 2.2) taking into account the ‘hidden’ symmetry breaking^{17,28,29} in β -PdBi₂: Even though the atomic arrangement in these crystals is globally centrosymmetric, electrons at Bi sites in neighbouring layers experience a locally non-centrosymmetric environment, which gives rise to a Rashba-like SOC^{44,45} and in-plane spin-momentum locking with opposite spin polarizations, see sketch in Fig. 4a. Because of the spin polarization, an in-plane magnetic field produces anisotropic splitting of the energy bands, which is large where \mathbf{B} is aligned with the spin-orbit field (for momenta orthogonal to \mathbf{B}), Fig. 4a, and very small where the two are perpendicular. As the result, opposite- \mathbf{k} states have parallel spin polarizations and can be expected to favour equal-spin (triplet) pairing with nodes along the direction of \mathbf{B} .

Figure 4a shows the free energy $F(\psi, \eta, B, T)$ calculated using separate gap equations for each Zeeman-split band for two pairing channels (with the s -wave order parameter ψ and a spin-polarised triplet order parameter η), see Methods and Supplementary Notes 2.3-2.5 for details. At low B , the s -wave state has lower energy and superconductivity is gradually suppressed by the magnetic field. However, as B

increases above a critical value ($\sim 0.7 B_{c2}^{s\text{-wave}}$ for the interaction parameters in Fig. 4a), the free energy of the s -wave state becomes larger than for the triplet state, resulting in a first-order phase transition to the triplet state. By minimising the free energy $F(\psi, \eta, B, T)$ for ψ and η , we have obtained the ground state mean-field configuration at each (B, T) and constructed a phase diagram (Fig. 4b) which shows that a transition from s -wave to triplet state occurs at the T -independent transition field B^* . The value of B^* depends on the parameters of the model, in particular, on the interaction parameters U and V for s -wave and p -wave pairing, respectively. In general, as V increases at fixed U , the transition to nodal superconductivity occurs at a lower B . In the limit $V \gg U$, B^* vanishes and nodal superconductivity is favourable at all magnetic fields. The values of U and V for β -PdBi₂ can be estimated from the experimental critical temperatures $T_c^{s\text{-wave}}$ and $T_c^{p\text{-wave}}$. For the ~ 80 nm thick PdBi₂ crystal we found $T_c^{s\text{-wave}} \approx 3$ K (Fig. 1e) and $T_c^{p\text{-wave}} \approx 2.4$ K (here $T_c^{p\text{-wave}}$ is taken as an extrapolation to $B = 0$ in Fig. 2d). Using this result and the fact that T_c of a singlet superconductor is given by

$$k_B T_c = 1.13 \hbar \omega_D e^{-\frac{1}{N_0 U}} \quad (6)$$

we estimate $UN_0 = 0.26$. Here N_0 is the DoS per unit cell volume and the Debye frequency $\hbar \omega_D = 0.01$ eV is taken to be of the order of the largest phonon frequency for β -PdBi₂⁴⁶. The value of V can be estimated in a similar way, by replacing U in eq. (6) with $2^{-1} V \rho^2 / (1 + \rho^2)$, where $\rho = \alpha k_F / \epsilon$ and $k_F = \sqrt{2}(\mu m + \alpha^2 m^2 - (\alpha^4 m^4 + 2\alpha^2 m^3 \mu + \epsilon^2 m^2)^{1/2})^{1/2}$ is the Fermi wavevector of the 2D-like band for effective mass m , chemical potential μ , Fermi energy ϵ and Rashba SOC strength α . Using the same $\hbar \omega_D$ as above, we estimate $VN_0 = 0.78$, i.e., a similar order of magnitude as U , as can be expected for a realistic superconductor.

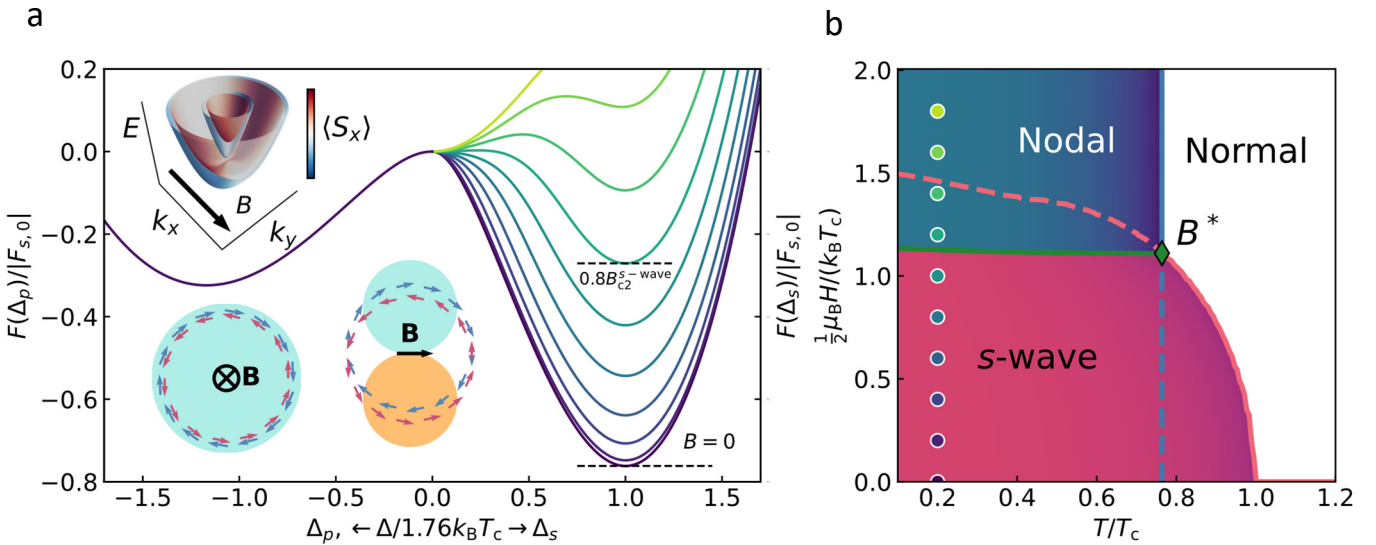


Figure 4 | Effect of the magnetic field on the free energy of s -wave and p -wave superconducting states of β -PdBi₂ and the corresponding phase diagram. **a**, Normalised free energy at $T = 0.1T_c$ for several values of the magnetic field (color-coded as indicated by dots in (b)) as a function of two possible order parameters: p -wave Δ_p in BCS units of $\Delta/1.76k_B T_c$ to the left of 0 (negative values) and s -wave Δ_s to the right. Within our model p -wave pairing is insensitive to the magnetic field. *Bottom-left inset*: Isotropic lift of band degeneracy due to out-of-plane magnetic field. States of opposite momenta have opposite spin polarizations, favoring s -wave coupling. *Top and bottom-right insets*: Anisotropic lift of band degeneracy due to the in-plane magnetic field. States of opposite momenta perpendicular to the direction of \mathbf{B} have parallel spin polarization, favoring p -wave coupling. **b**, Phase diagram constructed by minimising the free energy $F(\psi, \eta, B, T)$ for the s -wave order parameter ψ and a spin-polarised triplet order parameter η . Transition to the nodal p -wave state occurs at a temperature independent field B^* . Colored dots indicate the values of B corresponding to the free energy curves shown in (a).

Our experimental observations are in agreement with the predicted first-order phase transition from s -wave to triplet nodal pairing. A suppression (but not closing) of the s -wave gap in Fig. 3a is consistent with the appearance of nuclei of a new phase (nodal pairing) at B^* , as expected for a first-order phase transition. Furthermore, the apparent critical field for the s -wave phase (referred to as $B_c^{s\text{-wave}} \approx 0.25\text{T}$ in Fig. 3) is larger than B^* because the latter corresponds to the appearance of first nuclei of the new phase, while the superconductor becomes ‘fully p -wave’ only at fields well above B^* . In the example of Fig. 3a the new phase takes over at $B \sim 0.4\text{T}$ or $\sim 2B^*$. In the intermediate field range the two phases coexist, which can also explain why the tunnelling spectra here are described equally well by both the s -wave and the nodal order parameter. Let us emphasise that it would be incorrect to treat $B_c^{s\text{-wave}} \approx 0.25\text{T}$ in Fig. 3 as a true critical field for s -wave superconductivity because of the existence of the transition to p -wave pairing. Rather, the interaction between the two pairings for the in-plane field suppresses s -wave superconductivity at a much lower B than what would be the case without it (or what is observed in the out-of-plane B , where the material remains superconducting up to $\sim 1\text{T}$, Fig. 2d).

We note that the free energy in Fig. 4 does not include orbital depairing, leading to an unphysical result that $T_c^{p\text{-wave}}$ above B^* is independent of the magnetic field and $B_{c2}^{p\text{-wave}}$ diverges. Additionally, $B_{c2}^{s\text{-wave}}$ is equal to the Pauli paramagnetic limit (Fig. 4b), much higher than the experimental values, where orbital depairing dominates. Nevertheless, assuming that both s -wave and p -wave superconductivity are suppressed by orbital depairing in a similar way, our model correctly captures the fact that the transition to nodal pairing (for realistic parameters U and V) occurs well below $B_{c2}^{s\text{-wave}}$, as observed experimentally. Finally, we note that triplet pairing is unfavoured when the magnetic field is out-of-plane. This agrees with the experiment, where the pairing transition is induced by the in-plane, but not out-of-plane B .

The bilayer Rashba model discussed above and described in detail in Supplementary Notes 2.2-2.4 is the simplest model that reproduces all main features of $\beta\text{-PdBi}_2$ band structure, including the nontrivial spin helicity of the bulk and surface states. In turn, a p -wave triplet phase is the simplest nodal phase that emerges in this model and triggers a phase transition that can explain the experimental observations. Electronic states of a cylindrical Fermi surface can be described by a continuum Hamiltonian. We then assume two competing interactions: a local (Hubbard) and a non-local that couples electrons sitting on nearest-neighbouring sites that belong to different layers. The only allowed pairing channels here are nodeless s -wave states, an odd-parity pair density wave (PDW) state that changes sign each sublayer, and the $|m_L| = 0$ and $|m_L| = 1$ spin-triplet states⁴⁷. While the PDW and $|m_L| = 0$ triplet phases have point nodes at $k_x = k_y = 0$ and are therefore not compatible with the experimental spectra⁴¹, the only ones that host nodal lines are components of the $|m_L|=1$ triplet pairing. This effectively p -wave triplet phase is therefore the simplest nodal phase that can exist in this system. We note that higher symmetry d -wave states can also have nodal lines, but they are not compatible with the type of interaction assumed in our simple model, and one would have to consider more contrived non-local interactions to stabilise such phases. Let us also emphasise the role of the in-plane magnetic field: It can induce a substantial modification of the band structure in $\beta\text{-PdBi}_2$ because of the spin-momentum locking, which itself is due to the strong spin-orbit coupling. In turn, the changes in the band structure make the effectively p -wave triplet phase more stable than the s -wave above a transition field, a result that is compatible with experimental observations. This dependence on the applied magnetic field also suggests that a singlet d -wave pairing may not be suitable to describe the observed transition, as a Zeeman field, that only affects the spin, would not distinguish between two singlet states, or favour one over the other.

The above discussion did not include our puzzling observation that the superconducting parameters (T_c , Δ , B_{c2}^{\parallel}) of PdBi_2 crystals with $d \leq 150$ nm are strongly dependent on d , with T_c decreasing from 3.6K to 1.8K as d is reduced from 140 to 50 nm, see Supplementary Fig. 6. In contrast, B_{c2}^{\parallel} for these crystals

is notably enhanced compared to the bulk ($d \sim 100\mu\text{m}$) to approximately $B_{c2}^{\parallel}(0) \approx 1.6\text{T}$ (Fig. 2d) vs bulk $B_{c2}^{\parallel}(0) \approx 0.8\text{T}$ (Supplementary Fig. 1a), corresponding to a strong enhancement of B_{c2}^{\parallel}/T_c ratio, or superconductivity becoming more robust against B^{\parallel} for thinner crystals. Also the transition field B^* appears to show a thickness dependence: it is about twice lower for 50 nm thick PdBi₂ compared to 80nm, while two devices of a similar thickness showed similar B^* . No thickness dependence could be detected for the out-of-plane field. As $T_c(d)$ for our thin crystals accurately follows the $1/d$ dependence (Supplementary Fig. 6), this implies that the order parameter must be modified near the surface⁴⁸, with the surface contribution increasing for thinner crystals. Surprisingly, in the case of PdBi₂ the effect sets in at ~ 50 times larger thicknesses compared to thin films of conventional superconductors (~ 100 nm vs 2-5 nm)^{48,49}, indicating a different underlying mechanism. A possible explanation for the suppression of T_c , the relative enhancement of B_{c2}^{\parallel} , and also a lower transition field B^* in thin crystals is that nodal p -wave superconductivity (that has lower T_c , Fig. 2d and 4b) may become more energetically favourable near the surfaces due to hybridization with topological surface states^{10,50} (recall that our calculations only considered the hidden symmetry breaking and spin polarisation of bulk electronic bands). In β -PdBi₂ topological surface states^{28,30} have the same in-plane spin polarisation as the bulk bands^{28,30}, therefore one can expect the overall effect of B^{\parallel} to be enhanced, allowing a transition to p -wave superconductivity at a lower B^* and suppressing the overall $\Delta(B, T)$. Detailed understanding of this effect is beyond our current work and requires further experiments using a broad range of crystal thicknesses and further development of theory.

We note that the mechanism responsible for the field-induced transition in β -PdBi₂ appears to be fundamentally different from the phase transitions in uranium-based heavy fermion superconductors, such as UPt_3 ⁵¹, UTe_2 ³ and $\text{U}_{1-x}\text{Th}_x\text{Be}_{13}$ ⁵². In the latter case superconductivity is due to f -electron pairing with large magnetic moments⁵³ compared to the 4d and 6p states in β -PdBi₂²⁶. Furthermore, the predominant theory for uranium-based superconductors is that all superconducting phases are odd-parity p -wave or f -wave with different pairing potentials (\mathbf{d} -vectors) including the zero-field state, where coupling to magnetic orders determines which state is energetically favourable^{2,41,54}. No magnetic orders have been detected in β -PdBi₂. In CeRh_2As_2 , another heavy fermion system with a field-induced transition^{20,21}, the symmetry and spin-orbit properties are remarkably similar to β -PdBi₂, and the transition is also believed to be even-to-odd parity⁵⁵. However, the presence of antiferromagnetic correlations in CeRh_2As_2 ⁵⁶ and the fact that it is B^{\perp} (rather than B^{\parallel}) that is enhanced above the Pauli limit²⁰ implies that the underlying mechanism must be different there, too.

Finally, a finite-momentum FFLO state⁵⁷⁻⁵⁹ would also give rise to an enhancement of B_{c2} and a spatially modulated Δ , resulting in normal regions which could be interpreted as nodes in tunnelling spectroscopy. However, such non-uniform superconductivity is usually energetically unfavourable and only exists for very large fields close to the Pauli limit, $B_p = 1.86 \text{ T/K} \times T_c$. For our β -PdBi₂ B^* and indeed B_{c2} are far below $B_p \approx 5.6 \text{ T}$. In transition metal dichalcogenides with strong out-of-plane Ising SOC, finite momentum pairing has been suggested at $B < B_p$ ^{23,60}. However, such a picture does not apply to β -PdBi₂ where SOC is Rashba-type. In contrast, our simple model captures all features of the experimentally observed transition.

Methods

Crystal growth and characterisation

Single crystals of β -PdBi₂ were grown using a melt growth method. Pd and Bi in a molar ratio of 1:2 were sealed in an evacuated quartz tube and kept at high temperature (1050° C) for 6 hours to ensure complete melting and mixing of the components. The temperature was then reduced to 920 °C at

50°C/hour, the molten mixture maintained at this temperature for 24 hours, then slowly cooled to 500°C at a rate of 3°C h⁻¹ and rapidly quenched into iced water. This produced cleavable single crystals, with flat surfaces as large as $\sim 6 \times 6$ mm² (Supplementary Fig. 1b). Once recovered from the quartz tube, the crystals were always handled in the argon atmosphere of a glovebox (O₂ < 0.1 ppm, H₂O < 0.1 ppm) to prevent surface degradation. Phase purity was confirmed by X-ray diffraction ($\lambda = 1.5418\text{\AA}$, Rigaku Smartlab), see Supplementary Fig. 1b. To confirm that no phase transformations or impurities were introduced during device fabrication (see below), one of the studied devices was used for cross-sectional analysis in a scanning transmission electron microscope (STEM). To this end we used the well-known *in situ* ‘lift-out’ method⁶¹ and low-kV ion beam polishing⁶² to prepare a thin slice of the β -PdBi₂ crystal removed from the active area of a SiO₂-PdBi₂-hBN-FLG stack, perpendicular to the Bi-Pd-Bi layers. The thin slice of material was then transferred to a specialist Omniprobe TEM support grid and mounted with the incident electron beam perpendicular to the plane of the lamella. The resulting STEM image shows a cross-section of the active region of the device, with a perfect arrangement of Bi and Pd atoms, see Fig. 1d in the main text.

Magnetization measurements

Magnetization measurements were carried out using a commercial SQUID magnetometer MPMS XL7 (Quantum Design). Samples for these measurements (that we refer to as ‘bulk’) were cleaved off the same melt-grown β -PdBi₂ crystal as the one used to fabricate tunnel junctions. Typical sample dimensions for magnetisation measurements were (0.01-0.1)×4×4 mm. Prior to being placed in the magnetometer, samples were mounted inside low-magnetic background plastic straws, taking care to protect them from exposure to air. In zero-field-cooling (ZFC) mode of DC measurements the sample was first cooled down to the lowest available temperature (1.8 K) in zero magnetic field, then a finite field B applied and magnetisation $M(B)$ measured as a function of an increasing temperature T . In field-cooling (FC) mode, a field B was applied above T_c (typically at 10-15 K) and magnetisation measured as a function of decreasing T . The superconducting fraction was found as $f = (1 - N) 4\pi |dM/dH| / V$, where N is the demagnetisation factor and V the sample’s volume. This yielded $f = 1$, i.e., all our crystals were 100% superconducting.

The superconducting coherence length ξ and magnetic field penetration depth λ were found from the measured critical fields B_{c1} and B_{c2} using the standard expressions⁶³ $B_{c2} = \Phi_0/2\pi\xi^2$ and $B_{c1} = (\Phi_0/4\pi\lambda^2)[\ln k + \alpha(k)]$, where $\alpha(k) = 0.5 + (1 + \ln 2)/(2k - \sqrt{2} + 2)$. The measured critical fields (Supplementary Fig. 1a) were accurately reproducible for all studied crystals and did not depend on the crystal thickness in this ‘bulk’ limit (thickness d between 10 and 100 μm). At the lowest measurement temperature $T=1.8\text{K}$ we found $B_{c1}(1.8\text{K}) = 7$ mT, $B_{c2}^{\parallel}(1.8\text{K}) = 0.68$ T, $B_{c2}^{\perp}(1.8\text{K}) = 0.56$ T. The upper critical field for these crystals, $B_{c2}(T)$, is accurately described by the standard WHH theory⁶⁴, see inset in Supplementary Fig. 1a, yielding extrapolated values $B_{c2}^{\parallel}(0) \approx 0.9$ T and $B_{c2}^{\perp}(0) \approx 0.74$ T and a corresponding in-plane coherence length $\xi_{\text{ab}}(0) \approx 22$ nm. Low- T penetration depth was estimated using $B_{c1}(0) \approx 9$ mT, $\lambda(0) \approx 240$ nm.

Device fabrication

The layered nature of β -PdBi₂ allows it to be exfoliated similarly to graphite and stacked with other van der Waals materials. To build planar SIN tunnel junctions we used 50-140 nm thick PdBi₂ crystals as the superconducting electrode, 2-3 layer thick hBN as an atomically-flat tunnel barrier and few-layer graphene (FLG) as the normal metal, see schematic and an image of a typical device in Fig. 1b,c. To this end we used a dry transfer ‘stamping’ method where PdBi₂, FLG and hBN were exfoliated individually onto Si/SiO_x wafers. As the first step, Polypropylene carbonate (PPC) was spin-coated on polydimethylsiloxane (PDMS) mounted on a glass slide. This assembly was then used to pick up ~ 25 nm

thick top encapsulating layer of hBN (see ref. ⁶⁵). This hBN crystal was then used to lift FLG strips from the Si/SiO_x substrate, followed by picking up of a 2-3 layer-thick hBN flake from the thicker hBN crystal deposited initially on the Si/SiO_x substrate (this served as the tunnel barrier). Finally, the assembled stack was deposited onto a suitable PdBi₂ flake by detaching it from PDMS/PPC stamp. Exfoliation of PdBi₂ and the final stacking step were carried out in the protective atmosphere of an Ar-filled glovebox, to avoid degradation in air. Finally, Cr/Au contacts to FLG or directly to the PdBi₂ crystal (Fig. 1) were patterned using electron beam lithography: the encapsulating hBN layer over the contact areas was removed using reactive ion plasma etching and Cr/Au contacts deposited by thermal evaporation. To ascertain that the fabrication procedure did not affect the quality and crystallinity of PdBi₂ we used cross-sectional transmission microscopy as described in section 1.

As explained in the main text, we studied a relatively narrow range of thicknesses of PdBi₂ crystals in our tunnelling devices, with 50 nm being the thinnest. It would be interesting to also study much thinner, atomically thin, β -PdBi₂ but mechanical exfoliation of this material is, unfortunately, difficult. Our many attempts to produce crystals thinner than 50 nm were unsuccessful, as each successive exfoliation step made the crystals thinner but also smaller, with lateral dimensions quickly becoming less than a couple of microns and so unsuitable for making a device.

Tight binding Hamiltonian

Electronic states at the Fermi surface of β -PdBi₂ originate primarily from Bi p-orbitals and exhibit spin-momentum locking due to the strong atomic spin-orbit coupling (SOC)^{26,28}. Accordingly, we model β -PdBi₂ as a stack of Bi bilayers and construct a minimal tight-binding model from Bi p-orbitals (details of the model in Supplementary Note 2.2). We focus on the bulk bands with clear 2D character, i.e., those that generate Fermi surfaces that are nearly flat in the direction orthogonal to PdBi planes and originate from (predominantly) in-plane Bi orbitals that are only weakly hybridized with those of neighbouring bilayers. Due to the globally centrosymmetric atomic arrangement in 3D crystals of β -PdBi₂, Bi bands exhibit a twofold sublayer degeneracy. However, electrons at Bi sites experience a locally non-centrosymmetric environment⁴⁴. The local crystal field couples in-plane and out-of-plane Bi p-orbitals and, in combination with the atomic SOC, $\lambda L \cdot S$, gives rise to a Rashba-like SOC⁴⁴ and in-plane spin-momentum locking at the Fermi surface. Since Bi atoms of different sublayers are related by inversion symmetry (Supplementary Fig. 7), their electrons experience opposite crystal fields and Rashba-like SOCs. Therefore, the twofold degenerate bands exhibit opposite in-plane helical spin polarizations (see the sketch in Fig. 4a). As briefly discussed in the main text, it is the spin helicity of the bulk bands at the Fermi surface that plays a major role in the response of β -PdBi₂ superconductivity to magnetic fields. To study this effect in detail with semi-analytical techniques, we have derived a continuum model by expanding the 2D-like Bi band structure at the Fermi surface up to second order in wavevector \mathbf{k} around the Γ point. To simplify the problem as much as possible, we ignore the warping terms that give rise to a square-like Fermi surface, as well as the \mathbf{k} -dependent interlayer hopping terms. This results in a circularly symmetric Fermi surface. Including a Zeeman term due to the magnetic field, the resulting continuum Hamiltonian reads

$$H_0 = \frac{k^2}{2m} - \mu - \epsilon \sigma_x + \alpha \sigma_z (k_x s_y - k_y s_x) - h s_x, \quad (7)$$

where α is the Rashba spin-orbit strength, m the effective mass, μ the chemical potential, ϵ the hopping parameter between Bi sublayers and h the Zeeman energy. In this equation, s_i and σ_i ($i = x, y, z$) are Pauli matrices operating on the spin and sublayer degrees of freedom, respectively. We use $\alpha = 0.81$ eV, $m = -0.43$ eV⁻¹ and $\epsilon = 0.63$ eV, which reproduce the bands around the Γ point well. The typical value of the chemical potential is $\mu = -2.22$ eV. Next we consider the effect of the following interaction Hamiltonian:

$$H_{\text{int}} = -U (n_1^2 + n_2^2) - 2V n_1 n_2, \quad (8)$$

where n_i is the electron density in the Bi sublayer i , and U and V are local (Hubbard-like) and interlayer density-density interactions, respectively. While U allows only s -wave (spin-singlet) pairing, V enables also spin-polarised pairing, since paired electrons on different layers can have aligned spins. We apply a mean-field decomposition to H_{int} into two candidate pairing channels by introducing an s -wave order parameter ψ and a spin-polarised order parameter η . Both ψ and η pair electrons with opposite momenta; electrons paired by η have parallel spins. The calculated free energies for s -wave and triplet states are presented and discussed in the main text.

Fitting tunnelling data

In zero field, the suppression of PdBi_2 superconductivity with increasing T shows standard BCS behaviour, with coherence peaks at $eV_b = \pm\Delta$, as seen in the $G(V_b, T)$ in Fig. 1f. To extract the gap values, $\Delta(T)$, from measured individual spectra, these were first normalized by dividing by $G(V_b, T > T_c)$, i.e., by the spectra measured in the same range of V_b above T_c . We then calculated the DoS using eq. (2) in the main text and numerically integrated with the Fermi-Dirac derivative, eq. (1), for a given set of trial parameters (Δ, Γ). This procedure was repeated iteratively to find the parameters that minimized the sum of square residuals between the model and the data, and to extract $\Delta(T)$ shown in Fig. 1e.

To analyse the dependence of the measured spectra on B , we followed the theory developed by Maki³⁷ which itself used the theoretical framework formulated earlier by Abrikosov and Gor'kov⁶⁶ and Skalski et al.⁶⁷ for the DoS of a superconductor with magnetic impurities. A unifying concept in these theories is a time-reversal breaking perturbation caused by either the applied field or magnetic impurities⁴³. Early tunnelling experiments on thin films of conventional s -wave superconductors in parallel magnetic field^{38,39} showed that the field modifies not only the energy gap but also the functional form of the DoS, in excellent agreement with the Maki theory. In this scenario the superconducting DoS is $N(E) = N_{\uparrow}(E) + N_{\downarrow}(E)$, where $N_{\uparrow\downarrow}$ is the DoS for each spin species given by

$$\frac{N_{\uparrow\downarrow}(E)}{N_N(0)} = \frac{1}{2} \text{sgn}(E) \text{Re} \left(\frac{u_{\pm}}{\sqrt{u_{\pm}^2 - 1}} \right), \quad (9)$$

where the parameter u_+ (u_-) corresponds to spin up (spin down) and must be determined self-consistently from the equation

$$u_{\pm} = \frac{E \mp \mu B}{\Delta} + \frac{\zeta_{\pm}}{\sqrt{1 - u_{\pm}^2}}. \quad (10)$$

Here μB is the Zeeman energy and ζ parametrizes the orbital pair breaking due to breaking of time-reversal symmetry. To calculate the DoS for a given set of parameters (Δ, B, ζ), we numerically solved eqs. (8),(9) at each E to give $N(E)$. The conductance is then given by eq. (1) in the main text, similar to the zero-field case. The g -factor of $\beta\text{-PdBi}_2$ is ≈ 2 and the externally applied field penetrates our ~ 100 nm thick crystals uniformly, so we can set $\mu = \mu_B$ (Bohr magneton) and take B in (9) equal to the applied field B^{\parallel} . We are then left with only two fitting parameters, (Δ, ζ); their field dependences $\Delta(B)$ and $\zeta(B)$ can be found by solving simultaneously the transcendental equations³⁹

$$\zeta = \frac{1}{2} \left(\frac{\Delta_0}{\Delta} \right) \left(\frac{B}{B_{c2}} \right)^2 \quad (11)$$

$$\ln\left(\frac{\Delta}{\Delta_0}\right) = \begin{cases} -\frac{1}{4}\pi\zeta, & \zeta \leq 1 \\ -\cosh^{-1}(\zeta) - \frac{1}{2}\left[\zeta \sin^{-1}\left(\frac{1}{\zeta}\right) - \sqrt{1 - \frac{1}{\zeta^2}}\right], & \zeta > 1 \end{cases} \quad (12)$$

where $\Delta_0 \equiv \Delta(B = 0)$. The solution for $\zeta(B)$ shows that ZBC is only nonzero when $\zeta > 1$ which occurs at $B/B_{c2} > \sqrt{2}e^{-\frac{\pi}{8}} \approx 95\%$ ^{39,43,67}. In real s -wave superconductors the value of ζ can be higher for equivalent B (green dashed line in Fig. 3c) due to finite mean-free path effects^{38,39} but ZBC is still practically zero until $B/B_{c2} \approx 60\%$ as shown by the black dashed curve in Fig. 3d, in agreement with more detailed calculations by Strassler and Wyder⁶⁸. This is in clear contrast to our findings where ZBC increases almost immediately after the field reaches $B \sim B^*$, see Figs. 2c and 3d.

Let us note that the full Maki theory³⁷ contains one more term in eq. (9) taking into account the effect of spin-orbit scattering. However this term only needs to be included for large Zeeman splitting, such that $\mu_B B \gg \Delta$ or $B > 10\text{T}$ ⁶⁹, and is therefore not relevant for $\beta\text{-PdBi}_2$.

In the low-field regime $B < B^*$ the Maki theory provides accurate fits to our experimental spectra and $\zeta(B)$ almost exactly follows the form predicted by eqs. (11)-(12) if we set $B_c^{s\text{-wave}} = 0.25\text{ T}$, see Supplementary Fig. 5 for details. On the other hand, attempting to apply the Maki theory to the ‘V’-shaped spectra at $B > B^*$ results in poor fits even if $\zeta(B)$ is treated as a fitting parameter and allowed to take on unphysically large values compared to theory expectations for the corresponding range of B/B_{c2} , see Supplementary Fig. 5b (here $B_{c2} \approx 1.6\text{T}$ is the actual experimentally measured critical field). Using the theoretically predicted values of $\zeta(B)$ at $B > B^*$ (green dashed line in Fig. 3c) results in large discrepancies between the expected and observed spectra.

In contrast, nodal DoS (Supplementary Note 2.1) fits the data at $B > B^*$ well, see Fig. 3b and Supplementary Fig. 5b. Here we use a known approach to analysing tunnelling spectra of unconventional superconductors by incorporating all pair-breaking effects into a field-dependent imaginary part of the self-energy, Γ , by analogy with the zero-field Dyne’s model, and extract $\Delta(B)$ and $\Gamma(B)$ for each spectrum above B^* using eq. (3). As illustrated in Supplementary Fig. 3d,e, the effect of Γ in this case is to increase the ZBC already at low B , unlike the result of the s -wave Maki theory. This agrees qualitatively with calculations for specific pair-breaking perturbations in e.g. heavy fermion superconductors⁷⁰.

Data availability. The authors declare that the data supporting the findings of this study are available within the paper and its supplementary information files.

Code availability. The software code used in this work is available as a supplementary information file.

References

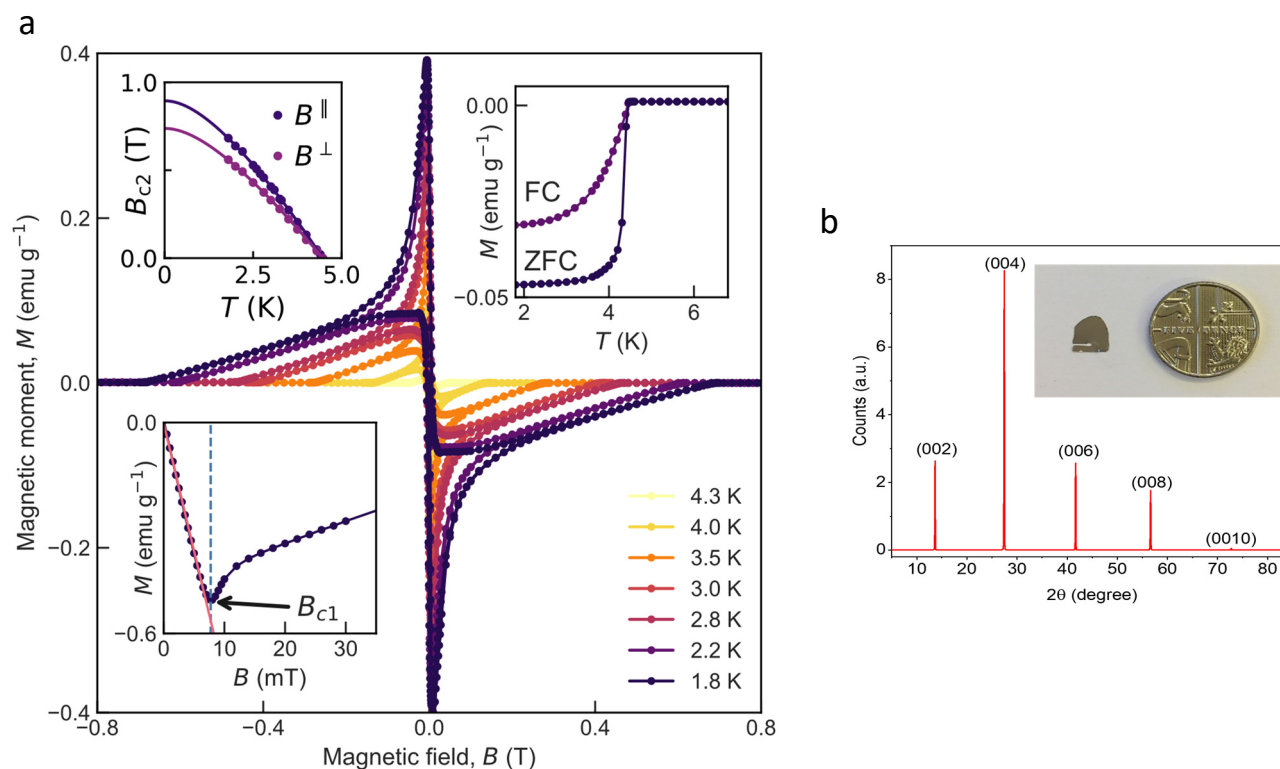
1. Leggett, A. J. A theoretical description of the new phases of liquid ^3He . *Rev. Mod. Phys.* **47**, 331–414 (1975).
2. Joynt, R. & Taillefer, L. The superconducting phases of UPt_3 . *Rev. Mod. Phys.* **74**, 235–294 (2002).
3. Hayes, I. M. *et al.* Multicomponent superconducting order parameter in UTe_2 . *Science* **373**, 797–801 (2021).
4. Ott, H. R., Rudigier, H., Fisk, Z. & Smith, J. L. Phase transition in the superconducting state of $\text{U}_{1-x}\text{Th}_x\text{Be}_{13}$ ($x=0-0.06$). *Phys. Rev. B* **31**, 1651–1653 (1985).
5. Ran, S. *et al.* Nearly ferromagnetic spin-triplet superconductivity. *Science* **365**, 684–687 (2019).
6. Lévy, F., Sheikin, I., Grenier, B. & Huxley, A. D. Magnetic field-induced Superconductivity in the ferromagnet URhGe . *Science* **309**, 1343–1346 (2005).
7. Ran, S. *et al.* Extreme magnetic field-boosted superconductivity. *Nat. Phys.* **15**, 1250–1254 (2019).
8. Aoki, D. *et al.* Extremely large and anisotropic upper critical field and the ferromagnetic instability in UCoGe . *J. Phys. Soc. Jpn.* **78**, 113709 (2009).

9. Vollhardt, D. & Wolfle, P. *The superfluid phases of helium 3*. (Dover Publications, Incorporated, 2013).
10. Kuang, W. *et al.* Magnetization signature of topological surface states in a non-symmorphic superconductor. *Adv. Mater.* **33**, 2103257 (2021).
11. Nadeem, M., Fuhrer, M. S. & Wang, X. The superconducting diode effect. *Nat. Rev. Phys.* **5**, 558–577 (2023).
12. de la Barrera, S. C. *et al.* Tuning Ising superconductivity with layer and spin–orbit coupling in two-dimensional transition-metal dichalcogenides. *Nat. Commun.* **9**, 1427 (2018).
13. Lu, J. M. *et al.* Evidence for two-dimensional Ising superconductivity in gated MoS₂. *Science* **350**, 1353–1357 (2015).
14. Xi, X. *et al.* Ising pairing in superconducting NbSe₂ atomic layers. *Nat. Phys.* **12**, 139–143 (2016).
15. Saito, Y. *et al.* Superconductivity protected by spin–valley locking in ion-gated MoS₂. *Nat. Phys.* **12**, 144–149 (2016).
16. Kuzmanović, M. *et al.* Tunneling spectroscopy of few-monolayer NbSe₂ in high magnetic fields: triplet superconductivity and Ising protection. *Phys. Rev. B* **106**, 184514 (2022).
17. Fischer, M. H., Sigrist, M., Agterberg, D. F. & Yanase, Y. Superconductivity and local inversion-symmetry breaking. *Annu. Rev. Condens. Matter Phys.* **14**, 153–172 (2023).
18. Yip, S. Noncentrosymmetric superconductors. *Annu. Rev. Condens. Matter Phys.* **5**, 15–33 (2014).
19. Gor’kov, L. P. & Rashba, E. I. Superconducting 2D system with lifted spin degeneracy: mixed singlet-triplet state. *Phys. Rev. Lett.* **87**, 037004 (2001).
20. Khim, S. *et al.* Field-induced transition within the superconducting state of CeRh₂As₂. *Science* **373**, 1012–1016 (2021).
21. Semeniuk, K. *et al.* Decoupling multiphase superconductivity from normal state ordering in CeRh₂As₂. *Phys. Rev. B* **107**, L220504 (2023).
22. Landaeta, J. F. *et al.* Field-angle dependence reveals odd-parity superconductivity in CeRh₂As₂. *Phys. Rev. X* **12**, 031001 (2022).
23. Zhao, D. *et al.* Evidence of finite-momentum pairing in a centrosymmetric bilayer. *Nat. Phys.* **19**, 1599–1605 (2023).
24. Zhuravlev, N. N. Structure of superconductors. X: thermal, microscopic and X-ray investigation of the bismuth-palladium system. *J Exptl Theor. Phys* (1957).
25. Imai, Y. *et al.* Superconductivity at 5.4 K in β -Bi₂Pd. *J. Phys. Soc. Jpn.* **81**, 113708 (2012).
26. Shein, I. R. & Ivanovskii, A. L. Electronic band structure and Fermi surface of tetragonal low-temperature superconductor Bi₂Pd as predicted from first principles. *J. Supercond. Nov. Magn.* **26**, 1–4 (2013).
27. Sakano, M. *et al.* Topologically protected surface states in a centrosymmetric superconductor β -PdBi₂. *Nat. Commun.* **6**, 8595 (2015).
28. Iwaya, K. *et al.* Full-gap superconductivity in spin-polarised surface states of topological semimetal β -PdBi₂. *Nat. Commun.* **8**, 976 (2017).
29. Zhang, X., Liu, Q., Luo, J.-W., Freeman, A. J. & Zunger, A. Hidden spin polarization in inversion-symmetric bulk crystals. *Nat. Phys.* **10**, 387–393 (2014).
30. Xu, T. *et al.* Nonhelical spin texture in the normal states of the centrosymmetric superconductor β -PdBi₂. *Phys. Rev. B* **100**, 161109 (2019).
31. Kačmarčík, J. *et al.* Single-gap superconductivity in β -Bi₂Pd. *Phys. Rev. B* **93**, 144502 (2016).
32. Biswas, P. K. *et al.* Fully gapped superconductivity in the topological superconductor β -PdBi₂. *Phys. Rev. B* **93**, 220504 (2016).
33. Herrera, E. *et al.* Magnetic field dependence of the density of states in the multiband superconductor β -Bi₂Pd. *Phys. Rev. B* **92**, 054507 (2015).
34. Soda, M. *et al.* Field dependence of superfluid density in β -PdBi₂. *J. Phys. Soc. Jpn.* **90**, 104710 (2021).
35. Tinkham, M. *Introduction to superconductivity*. (Dover Publications, 2004).
36. Dynes, R. C., Narayanamurti, V. & Garno, J. P. Direct measurement of quasiparticle-lifetime broadening in a strongly-coupled superconductor. *Phys. Rev. Lett.* **41**, 1509–1512 (1978).
37. Maki, K. Pauli paramagnetism and superconducting state. II. *Prog. Theor. Phys.* **32**, 29–36 (1964).
38. Millstein, J. & Tinkham, M. Tunneling into superconducting films in a magnetic field. *Phys. Rev.* **158**, 325–332 (1967).
39. Levine, J. L. Density of states of a short-mean-free-path superconductor in a magnetic field by electron tunneling. *Phys. Rev.* **155**, 373–378 (1967).
40. Worledge, D. C. & Geballe, T. H. Negative spin-polarization of SrRuO₃. *Phys. Rev. Lett.* **85**, 5182–5185 (2000).
41. Sigrist, M. & Ueda, K. Phenomenological theory of unconventional superconductivity. *Rev. Mod. Phys.* **63**, 239–311 (1991).
42. Fischer, Ø., Kugler, M., Maggio-Aprile, I., Berthod, C. & Renner, C. Scanning tunneling spectroscopy of high-temperature superconductors. *Rev. Mod. Phys.* **79**, 353–419 (2007).

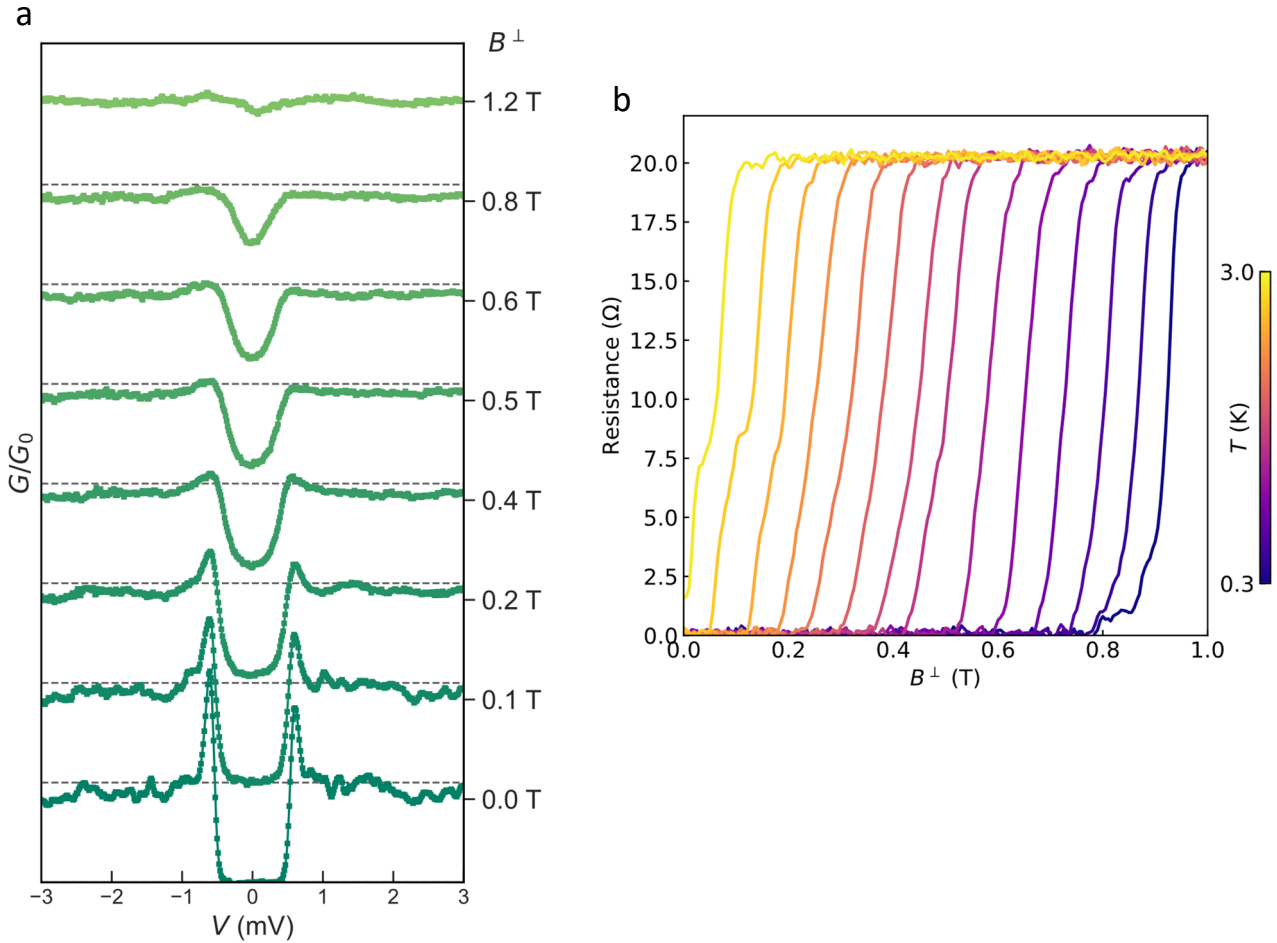
43. Maki, K. Gapless Superconductivity. in *Superconductivity: in two parts* (ed. R. D. Parks) vol. 2 (Routledge, 1969).
44. Petersen, L. & Hedegård, P. A simple tight-binding model of spin-orbit splitting of sp-derived surface states. *Surf. Sci.* **459**, 49–56 (2000).
45. Sigrist, M. *et al.* Superconductors with staggered non-centrosymmetry. *J. Phys. Soc. Jpn.* **83**, 061014 (2014).
46. Zheng, J.-J. & Margine, E. R. Electron-phonon coupling and pairing mechanism in β -Bi₂Pd centrosymmetric superconductor. *Phys. Rev. B* **95**, 014512 (2017).
47. Nakosai, S., Tanaka, Y. & Nagaosa, N. Topological superconductivity in bilayer Rashba system. *Phys. Rev. Lett.* **108**, 147003 (2012).
48. Simonin, J. Surface term in the superconductive Ginzburg-Landau free energy: application to thin films. *Phys. Rev. B* **33**, 7830–7832 (1986).
49. Khestanova, E. *et al.* Unusual suppression of the superconducting energy gap and critical temperature in atomically thin NbSe₂. *Nano Lett.* **18**, 2623–2629 (2018).
50. Kashiwaya, S., Tanaka, Y., Koyanagi, M. & Kajimura, K. Theory for tunneling spectroscopy of anisotropic superconductors. *Phys. Rev. B* **53**, 2667–2676 (1996).
51. Sauls, J. A. The order parameter for the superconducting phases of UPt₃. *Adv. Phys.* **43**, 113–141 (1994).
52. Ott, H. R., Rudigier, H., Felder, E., Fisk, Z. & Smith, J. L. Influence of impurities and magnetic fields on the normal and superconducting states of UBe₁₃. *Phys. Rev. B* **33**, 126–131 (1986).
53. Stewart, G. R. Heavy-fermion systems. *Rev. Mod. Phys.* **56**, 755–787 (1984).
54. Machida, K. Theory of spin-polarized superconductors - an analogue of superfluid ³He A-phase. *J. Phys. Soc. Jpn.* **89**, 033702 (2020).
55. Nogaki, K. & Yanase, Y. Even-odd parity transition in strongly correlated locally noncentrosymmetric superconductors: application to CeRh₂As₂. *Phys. Rev. B* **106**, L100504 (2022).
56. Kibune, M. *et al.* Observation of antiferromagnetic order as odd-parity multipoles inside the superconducting phase in CeRh₂As₂. *Phys. Rev. Lett.* **128**, 057002 (2022).
57. Wosnitza, J. FFLO states in layered organic superconductors. *Ann. Phys.* **530**, 1700282 (2018).
58. Larkin, A. & Ovchinnikov, Y. N. Nonuniform state of superconductors. *Sov. Phys.-JETP* **20**, 762–762 (1965).
59. Fulde, P. & Ferrell, R. A. Superconductivity in a strong spin-exchange field. *Phys. Rev.* **135**, A550–A563 (1964).
60. Liu, C.-X. Unconventional superconductivity in bilayer transition metal dichalcogenides. *Phys. Rev. Lett.* **118**, 087001 (2017).
61. Tomus, D. & Ng, H. P. In situ lift-out dedicated techniques using FIB-SEM system for TEM specimen preparation. *Micron* **44**, 115–119 (2013).
62. Schaffer, M., Schaffer, B. & Ramasse, Q. Sample preparation for atomic-resolution STEM at low voltages by FIB. *Ultramicroscopy* **114**, 62–71 (2012).
63. Brandt, E. H. Properties of the ideal Ginzburg-Landau vortex lattice. *Phys. Rev. B* **68**, 054506 (2003).
64. Werthamer, N. R., Helfand, E. & Hohenberg, P. C. Temperature and purity dependence of the superconducting critical field, H_{c2}. III. electron spin and spin-orbit effects. *Phys. Rev.* **147**, 295–302 (1966).
65. Pizzocchero, F. *et al.* The hot pick-up technique for batch assembly of van der Waals heterostructures. *Nat. Commun.* **7**, 11894 (2016).
66. Abrikosov, A. A. & Gor'kov, L. P. Contribution to the theory of superconducting alloys with paramagnetic impurities. *Zhur Eksptl Teor. Fiz* **39**, (1960).
67. Skalski, S., Betbeder-Matibet, O. & Weiss, P. R. Properties of superconducting alloys containing paramagnetic impurities. *Phys. Rev.* **136**, A1500–A1518 (1964).
68. Strässler, S. & Wyder, P. Effect of the mean free path on the magnetic behavior of small superconducting particles. *Phys. Rev.* **158**, 319–325 (1967).
69. Meservey, R., Tedrow, P. M. & Bruno, R. C. Tunneling measurements on spin-paired superconductors with spin-orbit scattering. *Phys. Rev. B* **11**, 4224–4235 (1975).
70. Ueda, K. & Rice, T. M. Heavy electron superconductors - some consequences of the p-wave Pairing. in *Theory of heavy fermions and valence fluctuations: proceedings of the eighth Taniguchi symposium, Shima Kanko, Japan, April 10–13, 1985* (eds. Kasuya, Tadao & Saso, Tetsuro) vol. 62 (Springer Science & Business Media, 2012).

SUPPLEMENTARY INFORMATION

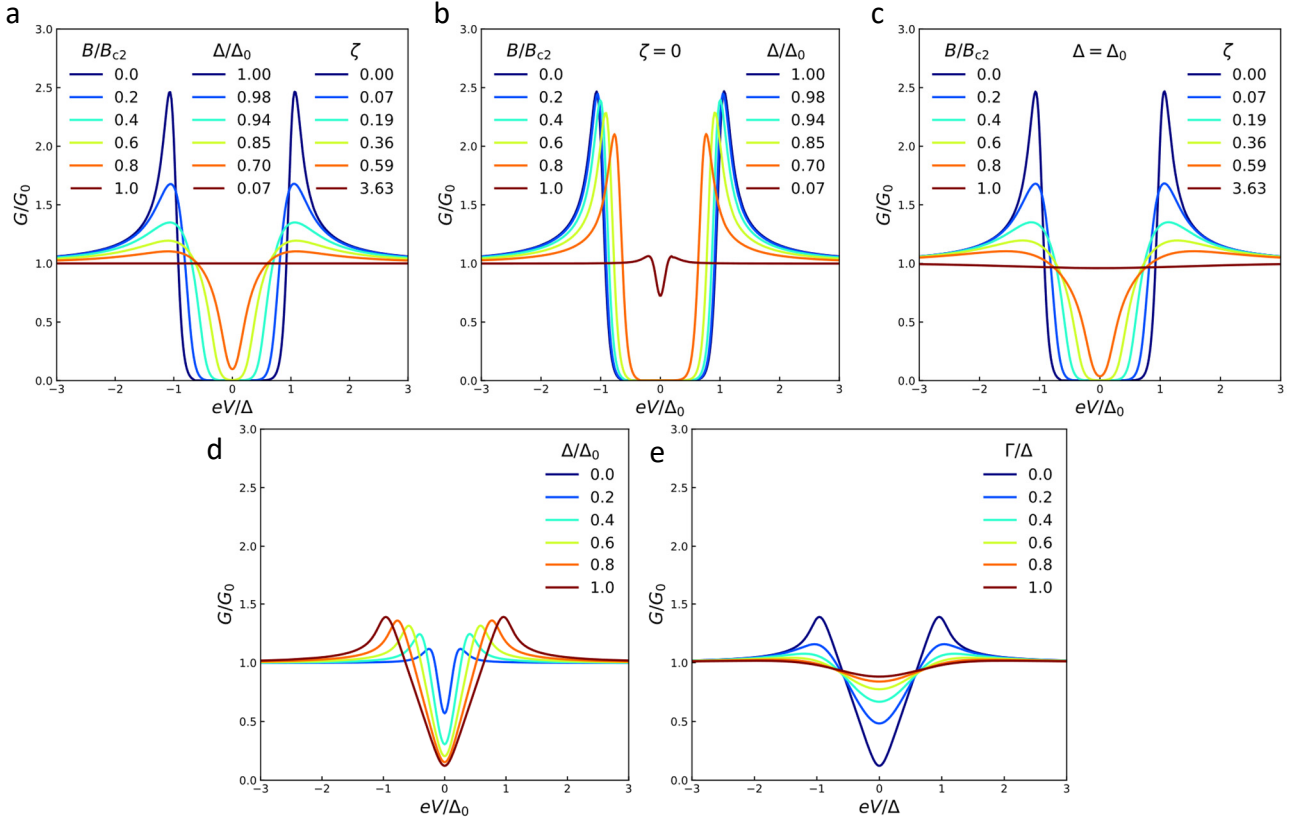
1. Supplementary Figures



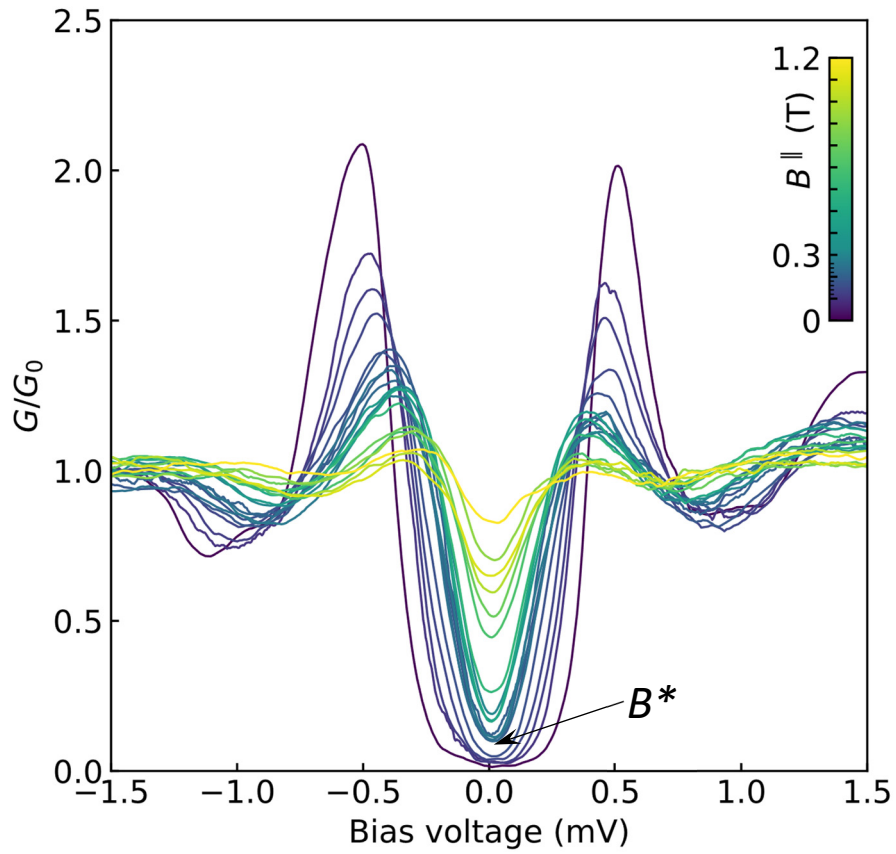
Supplementary Figure 1 | Characterization of bulk β -PdBi₂ crystals. Typical magnetization curves for bulk samples at different temperatures. Shown are data for a $\sim 100\mu\text{m}$ thick crystal. **a**, *Main panel*: Magnetisation vs applied magnetic field at several temperatures (see legend). *Lower left inset*: Zoom of the magnetisation curve at 1.8 K corresponding to vortex penetration at the lower critical field B_{c1} . *Upper left inset*: Temperature dependence of the upper critical field for in-plane and out-of-plane orientations of the applied B , see legend. Solid lines are fits to WHH theory. *Top right inset*: Superconducting transition as seen in dc magnetization of a $\sim 100\ \mu\text{m}$ thick crystal; $T_c = 4.5\ \text{K}$. Shown are field-cooling (FC) and zero-field cooling (ZFC) magnetization curves. **b**, X-ray diffraction pattern of our single crystals showing sharp (00l) peaks (FWHM 0.03°), accurately matching the β -phase of PdBi₂. The inset shows a typical flat section of the as-grown crystal used to exfoliate crystals for device fabrication.



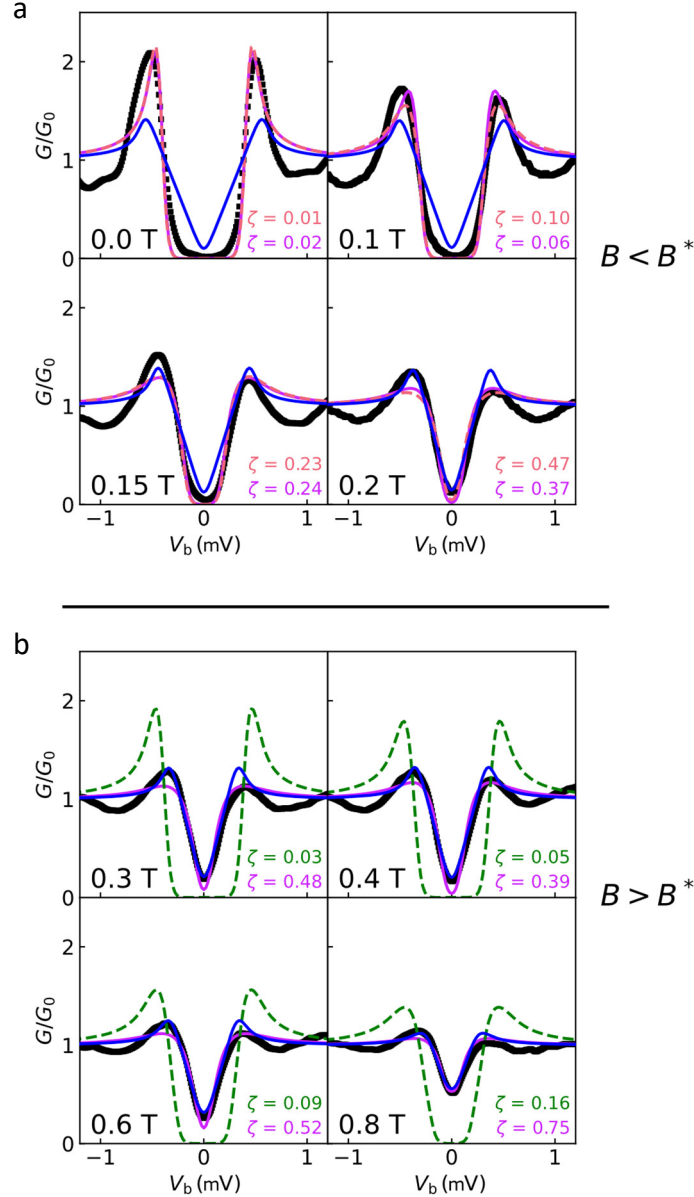
Supplementary Figure 2 | Evolution of the tunnelling spectra and device resistance in out-of-plane magnetic field. **a**, Tunnelling spectra measured at $T = 0.3\text{K}$ as a function of perpendicular field, B^\perp , see labels for field values. Data for device C. The spectra cannot be translated directly into the superconducting DoS due to an (unknown) contribution from the normal cores of vortices that penetrate the junction in this field range. **b**, Resistance R as a function of the out-of-plane field B^\perp , measured at different temperatures. Data for device A.



Supplementary Figure 3 | Modelling of the tunnelling spectra expected for *s*-wave and nodal *p*-wave superconductors in magnetic field. **a**, Evolution of the conductance spectra for an *s*-wave superconductor as a function of two parameters, order parameter Δ and pair-breaking strength ζ . The spectra are calculated using eqs. (9)-(12) in Methods (Maki theory). Legends show ζ and Δ computed for selected values of B/B_{c2} using eqs. (11),(12). The spectra demonstrate qualitative features of the effect of magnetic field as described in the main text: zero-bias conductance (ZBC) remains zero and the spectra are fully gapped up to $B \sim 0.7B_{c2}$; quasiparticle peaks are almost fully suppressed at $B > 0.5B_{c2}$. **b**, Same as (a) but only the order parameter Δ is allowed to vary, while $\zeta = 0$ for all B (see legends). This demonstrates that decreasing Δ changes the scale but not the shape of the spectra, except very close to the transition to the normal state, where thermal broadening becomes important. The relative insensitivity of the spectral shape to increasing B in this case follows from the Ginzburg-Landau dependence $\Delta(B) \sim \sqrt{(1 - B/B_{c2})^2}$, such that Δ is only suppressed close to B_{c2} . **c**, Same as (a) but with the order parameter fixed at $\Delta = \Delta_0$. Comparing (a) and (c) shows that the evolution of the spectral shape is mainly driven by the pair-breaking strength ζ : it reduces the gap and strongly suppresses the quasiparticle peaks, while ZBC remains zero for all but the largest values of $\zeta > 1$. **d-e**, Calculated evolution of the conductance spectra for a *p*-wave superconductor characterised by an order parameter with line nodes, eq. (3) in the main text. Panel (d) shows the effect of reducing Δ while the broadening parameter Γ is fixed at $\Gamma = 0$. Decreasing Δ changes the slope of the linear DOS inside the gap but has a weak effect on ZBC. Panel (e) shows the effect of an increasing Γ (equivalent to pair-breaking strength in the Maki model). Increasing Γ has a strong effect on the ZBC. In all panels the temperature is $T = 0.1\Delta/1.76k_B = 0.1T_c$, corresponding to experiment ($T = 0.3\text{K}$, $T_c \approx 3\text{K}$).

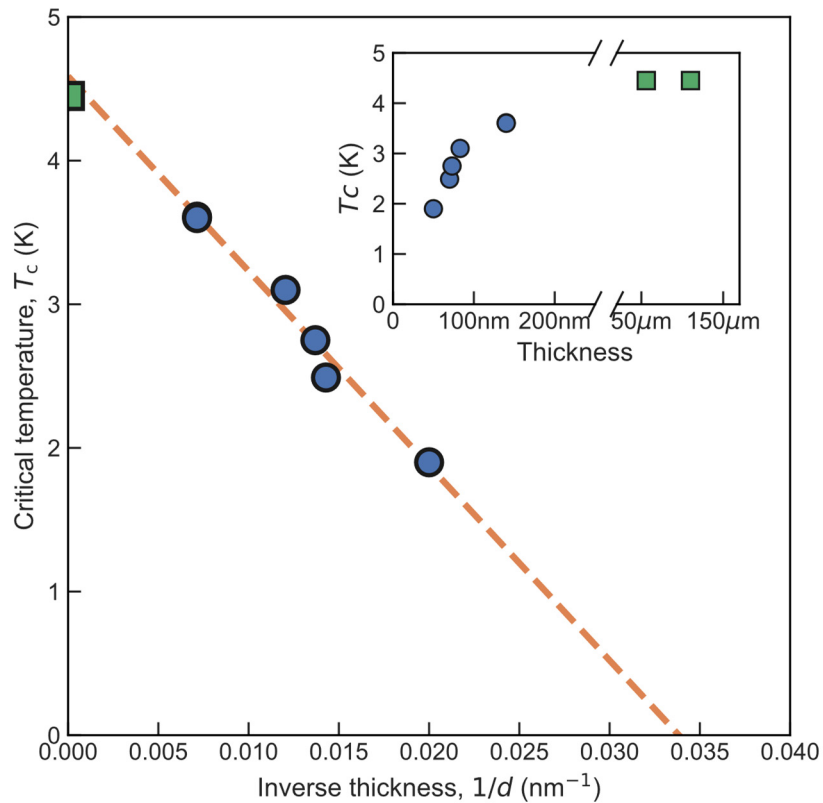


Supplementary Figure 4 | Evolution of the tunnelling spectra for in-plane magnetic field. Measured spectra are shown without a shift, to emphasise the change in spectral shape at B^* . Data for device B; $T = 0.3\text{K}$.



Supplementary Figure 5 | Analysis of the tunnelling spectra under in-plane magnetic field and comparison with theoretical models for s -wave and p -wave superconductivity. **a**, Representative tunnelling spectra for in-plane B^{\parallel} below the transition field B^* , and comparison to the two theoretical models. Black symbols are data, magenta solid lines are best fits to the Maki theory with Δ and the pair-breaking ζ used as fitting parameters, and red dashed lines are spectra *calculated* from the Maki theory using $\Delta_0 = 0.44$ meV (as obtained from fitting at $B = 0$) and $B_c^{S\text{-wave}} = 0.25$ T extrapolated from $\Delta(B^{\parallel})$ below B^* in Fig. 3a in the main text. Color-coded legends show corresponding values of the pair-breaking strength (calculated and obtained from the fit, respectively). Fitted and calculated spectra are practically indistinguishable and both accurately describe an s -wave superconductor (compare with panel (a) in Supplementary Fig. 3). In contrast, fits to a nodal gap (blue solid lines) are poor, except very close to B^* . **b**, Same for the spectra measured at $B^{\parallel} > B^*$. Green dashed lines show spectra that would be expected from the Maki theory for a ‘global’ upper critical field $B_{c2} = 1.6$ T (where PdBi₂ transitions to the normal state). Solid blue lines are best fits to the nodal model. For completeness, we also attempted fitting with the Maki model by allowing the pair-breaking strength to take on arbitrarily large values. These fits are shown by solid magenta lines and the corresponding values of the pair-breaking strength are shown by color-coded legends. It is clear that the spectra for all $B > B^*$ are best described by the

nodal DoS. Superficially, the Maki model also describes the spectra reasonably well but requires pair-breaking strength well beyond the values predicted by this theory – the latter are shown in the legends in green. We therefore conclude that the Maki model is not valid in this field range, while the assumption of the p -wave order parameter with line nodes provides an accurate fit to the experimental data.



Supplementary Figure 6 | Dependence of the transition temperature T_c on the thickness of PdBi_2 crystals. *Main panel:* Critical temperatures for different samples follow a $1/d$ dependence, where d is the crystal thickness. Blue circles are data obtained from $R(T)$ measurements on different tunnelling devices; green squares are data obtained from magnetisation measurements on bulk crystals ($d > 10 \mu\text{m}$). Inset shows the same data on linear scale.

2. Supplementary Notes

2.1. Density of states of a nodal superconductor

The low-energy excitation spectrum of a superconductor can be calculated from the Nambu-Gorkov Green's functions. In the absence of disorder and magnetic field the diagonal and off-diagonal parts are¹⁰

$$G(\mathbf{k}, i\epsilon_n) = \frac{i\epsilon_n + \xi_{\mathbf{k}}}{(i\epsilon_n)^2 - \xi_{\mathbf{k}}^2 - |\Delta_{\mathbf{k}}|^2}, \quad (\text{S1})$$

$$F(\mathbf{k}, i\epsilon_n) = \frac{\Delta_{\mathbf{k}}^\dagger}{(i\epsilon_n)^2 - \xi_{\mathbf{k}}^2 - |\Delta_{\mathbf{k}}|^2}. \quad (\text{S2})$$

Here, $\xi_{\mathbf{k}} = \frac{k^2}{2m}$ is the band energy and $\epsilon_n = \frac{(2n+1)\hbar\pi}{k_B T}$ the fermionic Matsubara frequency. For a p -wave superconductor with an order parameter $\Delta_{\hat{\mathbf{k}}} = \Delta \cos(\theta_{\mathbf{k}})$ the normalized DoS is given by

$$\begin{aligned} \frac{N_S(E, \Delta)}{N_0} &= -\frac{1}{N_0} \text{Im} \int_0^\infty \frac{dk k^2}{2\pi} \int \frac{d\Omega_{\mathbf{k}}}{4\pi} G(\mathbf{k}, i\epsilon_n) \Big|_{i\epsilon_n \rightarrow E+i\eta} \\ &= -\text{Im} \int \frac{d\Omega_{\mathbf{k}}}{4\pi} \int_{-\infty}^\infty d\xi \frac{i\epsilon_n + \xi_{\mathbf{k}}}{(i\epsilon_n)^2 - \xi_{\mathbf{k}}^2 - |\Delta_{\mathbf{k}}|^2} \Big|_{i\epsilon_n \rightarrow E+i\eta} \\ &= \text{Re} \int \frac{d\Omega_{\mathbf{k}}}{4\pi} \frac{E}{\sqrt{E^2 - \Delta^2 \cos^2(\theta)}} \\ &= \text{Re} \left[\frac{E}{\Delta} \arcsin \left(\frac{\Delta}{E} \right) \right], \end{aligned} \quad (\text{S3})$$

where $\Omega_{\mathbf{k}}$ is the solid angle spanned by the 3D unit vector $\hat{\mathbf{k}}$ and N_0 is the normal-state DoS. This expression is linear for $E < \Delta$ and gives rise to sharp but finite peaks at $E = \Delta$. The pair-breaking effect of the magnetic field and/or disorder can be included by replacing $E \rightarrow E + i\Gamma$ (see 'Fitting tunnelling data' in Methods) which yields

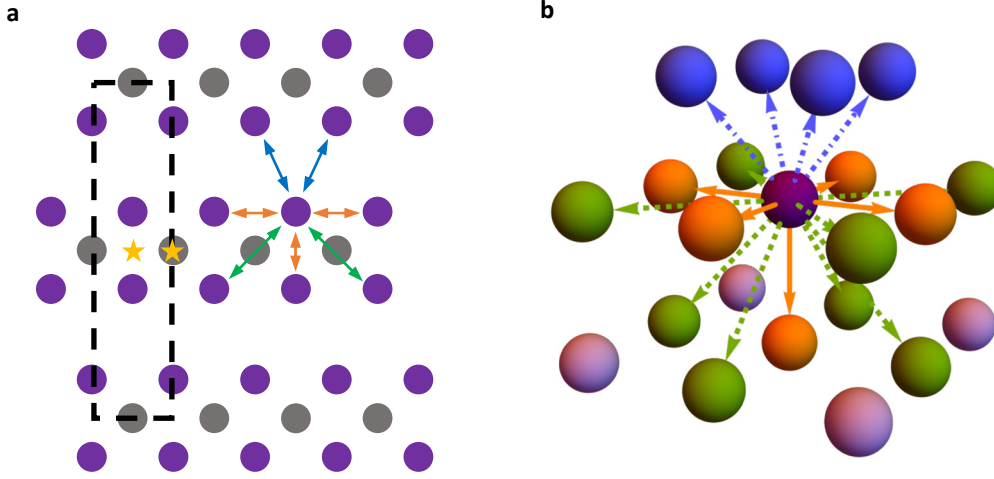
$$\frac{N_S(E, \Gamma, \Delta)}{N_0} = \text{Re} \left[\frac{E + i\Gamma}{\Delta} \arcsin \left(\frac{\Delta}{E + i\Gamma} \right) \right]. \quad (\text{S4})$$

2.2. Tight binding model

As shown in Supplementary Fig. 7, the crystal lattice of β -PdBi₂ is composed of covalently bonded trilayers held together by van der Waals forces. Each trilayer consists of an inner Pd square monolayer (grey atoms in Supplementary Fig. 7a) enclosed by two AA-stacked (atom-above-atom) square Bi monolayers (purple atoms in Supplementary Fig. 7a). We consider the two Bi monolayers within a trilayer as "sublayers" and label them with an index σ . Neighbouring trilayers are shifted such that the Bi atoms in one layer are lined up with the Pd sites in the other. Thus, the tetragonal crystal unit cell (black solid lines in Supplementary Fig. 7a) consists of six atoms, two Pd and four Bi. We now build three model Hamiltonians of different complexities:

- I. A 2D tight-binding model for a single Bi bilayer.
- II. A 3D tight-binding model built by stacking bilayers of model I, which allows comparing the results with literature.
- III. A 2D continuum model simplified from I, from which the superconducting gap equations used in this work are derived.

The 2D tight-binding model contains all symmetry-permitted hopping amplitudes between Bi sites up to next-nearest neighbours. The states that contribute to the Fermi surface are predominantly Bi p orbitals where hopping occurs between nearest- and next-nearest-neighbour atoms of each Bi bilayer (orange and green arrows in Supplementary Fig. 7a, respectively), as well as between Bi atoms of different bilayers (blue arrows in Supplementary Fig. 7a). These p -orbitals form intra-sublayer ‘sigma’ bonds with strength w and ‘pi’ bonds with strength δ . The inter-sublayer sigma and pi bonds have strength w' and δ' respectively. The effect of Pd d orbitals is captured by renormalising the Bi hopping parameters. The crystal field, $\pm\gamma$, couples p_z orbitals to the radial component, p_r , of neighbouring $p_{x,y}$ orbitals in the same sublayer. On the other hand, crystal-field-induced coupling between the two sublayers is forbidden, as Bi atoms from the sublayers are related by inversion symmetry.



Supplementary Figure 7 | Crystal structure and tight-binding description of β -PdBi₂. **a**, Side view of the atomic arrangement. Two Bi and one Pd monolayers forming each trilayer are covalently bonded, while neighbouring trilayers are held together by weaker van der Waals forces. *Dashed rectangle*: the unit cell. *Yellow stars*: inversion centers. Arrows indicate hopping amplitudes used in the tight-binding calculations. **b**, 3D view of the crystal composed of Bi trilayers with atoms color-coded according to the hopping amplitudes (same color coding as in (a)).

We work in a 12-dimensional basis, $|p_i, \sigma, s\rangle$ where $p_i \in \{p_x, p_y, p_z\}$ is the orbital basis, $\sigma \in \{A, B\}$ is the sublayer index and $s \in \{\uparrow, \downarrow\}$ is the spin index. The Hamiltonian of the system contains nearest-neighbour (NN), next-nearest neighbour (NNN) and spin-orbit coupling (SOC) terms and reads

$$H = h^{\text{NN}} + h^{\text{NNN}} + h^{\text{SOC}}. \quad (\text{S5})$$

Explicitly, the wavevector (\mathbf{k})-dependent NN couplings are given by

$$\begin{aligned} h_{xx}^{\text{NN}} &= 2w \cos k_x - 2\delta \cos k_y - \delta', \\ h_{yy}^{\text{NN}} &= 2w \cos k_y - 2\delta \cos k_x - \delta' \sigma_x, \\ h_{zz}^{\text{NN}} &= -2\delta(\cos k_x + \cos k_y) + w' \sigma_x, \\ h_{xz}^{\text{NN}} &= (h_{zx}^{\text{NN}})^* = 2i\gamma \sin k_x \sigma_z, \\ h_{yz}^{\text{NN}} &= (h_{zy}^{\text{NN}})^* = 2i\gamma \sin k_y \sigma_z, \end{aligned} \quad (\text{S6})$$

where the indexes $\alpha, \beta = x, y, z$ in $h_{\alpha\beta}^{\text{NN}}$ refer to the three p -orbitals and the Pauli matrices σ_x , σ_y and σ_z operate on the sublayer degree of freedom (terms that are not multiplied by a Pauli matrix are assumed to be proportional to the identity matrix). With a suitable choice of parameters w , w' , δ , δ' and γ , the

bands $E(k_x, k_y)$ obtained from h^{NN} within this minimal model resemble the known band structure of β -PdBi₂ along $\Gamma - X$, but fails to reproduce the bands along $\Gamma - M$ and $M - X$ ¹⁻⁴. Additionally, this minimal model exhibits a symmetry between the energy spectra at Γ and M points, $E(0,0) = -E(\pi, \pi)$, which is not present in the DFT and ARPES results for β -PdBi₂^{1,2}, implying that h^{NN} is missing essential terms.

The fact that the discrepancy lies in the direction of $M = (\pi, \pi)$ indicates that the missing terms describe hopping with a diagonal component, most naturally arising from hopping to intralayer NNN sites. Since these have a comparable distance to next-nearest inter-sublayer neighbours, we include both hoppings in h^{NNN} . The components of h^{NNN} are then given by

$$\begin{aligned}
h_{xx}^{NNN} &= 2(w'' - \delta'') \cos k_x \cos k_y + (a \cos k_x + b \cos k_y) \sigma_x, \\
h_{yy}^{NNN} &= 2(w'' - \delta'') \cos k_x \cos k_y + (a \cos k_y + b \cos k_x) \sigma_x \\
h_{zz}^{NNN} &= -4\delta'' \cos k_x \cos k_y + c(\cos k_x + \cos k_y) \sigma_x, \\
h_{xy}^{NNN} &= h_{yx}^{NNN} = -2(w'' + \delta'') \sin k_x \sin k_y, \\
h_{xz}^{NNN} &= (h_{zx}^{NNN})^* = 2\sqrt{2}i\gamma'' \sin k_x \cos k_y \sigma_z, \\
h_{yz}^{NNN} &= (h_{zy}^{NNN})^* = 2\sqrt{2}i\gamma'' \sin k_y \cos k_x \sigma_z.
\end{aligned} \tag{S7}$$

Here w'' and δ'' describe in-plane next-nearest neighbour hopping along diagonal intralayer π and σ bonds respectively. The parameters a , b and c denote hopping along some mixture of π and σ bonds between orbitals and their next-nearest inter-sublayer neighbours. Finally, γ'' denotes in-plane next-nearest neighbour diagonal hopping between $p_{x,y}$ and p_z atoms induced by the crystal field.

Both Hamiltonians h^{NN} and h^{NNN} are diagonal in spin. SOC can be included directly as $h^{SOC} = \lambda \mathbf{L} \cdot \mathbf{S}$, where L_i are the usual orbital angular momentum operators acting on the orbital basis and $S_i = s_i/2$ are the spin operators. The high atomic number of Bi implies that the spin-orbit coupling λ is large in this system due to relativistic effects. Indeed, the atomic SOC of Bi is estimated to be ~ 0.5 eV⁴.

2.3. 3D model

To compare our model with ARPES experiments and DFT calculations in the literature, we model a semi-infinite slab of β -PdBi₂ as a stack of square Bi bilayers with nearest-neighbour interactions by recursively coupling single-bilayer Green's functions and renormalising them into an effective surface slab. To this end we follow the efficient method of López Sancho et al⁵ that describes the surface of a 2^N -layer stack at step N . We write the semi-infinite Hamiltonian as the tridiagonal matrix,

$$\mathcal{H} = \begin{pmatrix} H & V & & \\ V^\dagger & H & V & \\ & V^\dagger & \dots & \dots \\ & & \dots & \dots \end{pmatrix}, \tag{S8}$$

where we neglect momentarily the NNN part of the Hamiltonian; thus $H = h^{NN} + h^{SOC}$. Here, V is the interlayer hopping which takes the form

$$V = v e^{-\frac{i(k_x + k_y)}{2}} \sigma_-, \tag{S9}$$

where $\sigma_\pm = (\sigma_x \pm i\sigma_y)/2$ and v is a matrix in the orbital basis with the following elements:

$$\begin{aligned}
v_{xx} &= v_{yy} = (2 \sin^2 \phi (w_v - \delta_v) - 4 \cos^2 \phi \delta_v) \cos \frac{k_x}{2} \cos \frac{k_y}{2}, \\
v_{zz} &= 4(\cos^2 \phi w_v - \sin^2 \phi \delta_v) \cos \frac{k_x}{2} \cos \frac{k_y}{2},
\end{aligned}$$

$$\begin{aligned}
v_{xy} = v_{yx} &= -2 \sin^2 \phi (w_v + \delta_v) \sin \frac{k_x}{2} \sin \frac{k_y}{2}, \\
v_{xz} = v_{zx}^* &= 2\sqrt{2}i \cos \phi \sin \phi (w_v + \delta_v) \sin \frac{k_x}{2} \cos \frac{k_y}{2}, \\
v_{yz} = v_{zy}^* &= 2\sqrt{2}i \cos \phi \sin \phi (w_v + \delta_v) \cos \frac{k_x}{2} \sin \frac{k_y}{2}.
\end{aligned} \tag{S10}$$

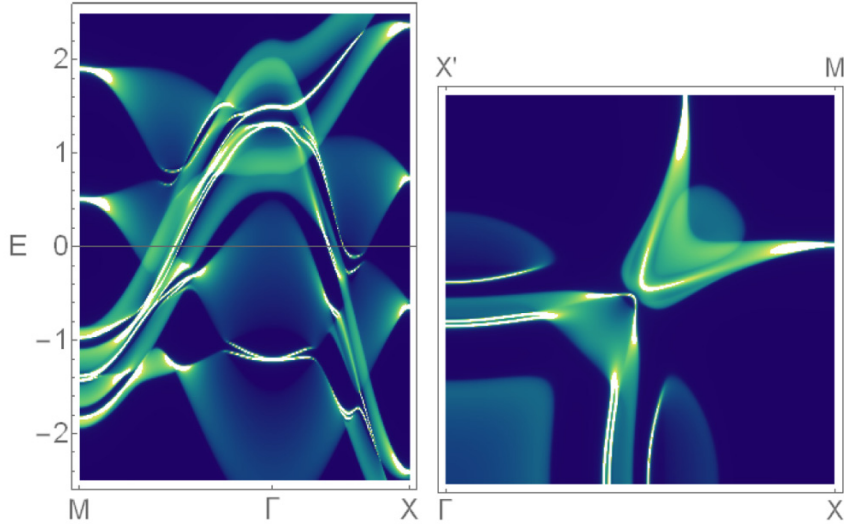
Here ϕ is the interlayer stacking zenith angle and w_v and δ_v are new parameters for interlayer hopping. The corresponding semi-infinite Green's function $\mathcal{G}(E, \mathbf{k})$ is defined by

$$(E - \mathcal{H}(\mathbf{k}))\mathcal{G}(E, \mathbf{k}) = \mathcal{I}, \tag{S11}$$

where \mathcal{I} is the identity operator. The surface spectral function takes the usual form

$$\mathcal{A}_S(E) = \text{Tr Im } G_S(\mathbf{k}, E - i\epsilon). \tag{S12}$$

The retarded surface Green's function, $G_S(\mathbf{k}, E - i\epsilon)$, can be obtained from the single-layer matrices H and V by iterating the decimation procedure described in ref. ⁵ until G_S converges to arbitrary precision. The calculated spectral function is shown in Fig. S3. The validity of our approximation is confirmed not just by the agreement of the bulk bands with the literature^{1,6}, but also by the presence of helical topological surface states^{1,6}.



Supplementary Figure 8. *Left:* Surface spectral function $A_S(\mathbf{k}, E)$ showing the band structure for \mathbf{k} along (M, Γ , X). *Right:* The same function at the Fermi level, $A_S(\mathbf{k}, 0)$ for \mathbf{k} in one quarter of the first Brillouin zone.

2.4. Continuum model for the p_r bands

To construct a minimal continuum model that describes the p_r bands with strong Rashba spin-orbit locking we rotate to a basis which is cylindrical in the orbital wavefunctions (p_z, p_r, p_θ). We begin by expanding our Hamiltonian to second order around Γ and then noticing that the Hamiltonian becomes block-diagonal by choosing $\psi_s = (|p_z \uparrow -\rangle, |p_z \downarrow +\rangle, |p_r \uparrow +\rangle, |p_r \downarrow -\rangle, |p_\theta \uparrow +\rangle, |p_\theta \downarrow -\rangle)$:

$$H\Psi = \begin{pmatrix} H_s & 0 \\ 0 & H_s \end{pmatrix} \begin{pmatrix} \psi_s \\ s_x \psi_s \end{pmatrix}, \tag{S13}$$

where $|p_i s \pm\rangle = |p_i s, \sigma = 1\rangle \pm |p_i s, \sigma = 2\rangle$. To further simplify the problem, we eliminate the p_θ and p_z bands using the Löwdin-Feshbach method⁷. The resulting 4×4 matrix is block-diagonal. The top 2×2 block in the basis ($|p_r \uparrow +\rangle, |p_r \downarrow -\rangle$) is given by

$$H_r = \begin{pmatrix} \frac{k^2}{2m_+} + \beta_+ k^2 \cos(4\theta) - \mu + \epsilon & ie^{-i\theta} k\alpha \\ -ie^{i\theta} k\alpha & \frac{k^2}{2m_-} + \beta_- k^2 \cos(4\theta) - \mu - \epsilon \end{pmatrix}. \quad (\text{S14})$$

The parameters $m_\pm, \beta_\pm, \mu, \epsilon$ and α are independent of k and are related in complex ways to the original parameters, while θ is the angle between the vector \mathbf{k} and the k_x direction.

We further simplify the Hamiltonian by assuming that the Fermi surface warping terms β_\pm are not significant and can be ignored. Furthermore, we also replace the difference between $\frac{k^2}{2m_+}$ and $\frac{k^2}{2m_-}$ by a constant that we absorb into ϵ , such that the separation of the two Fermi surfaces is preserved. We then recover the Rashba bilayer Hamiltonian⁸, which in the familiar basis ($|\uparrow, \sigma = 1\rangle, |\downarrow, \sigma = 1\rangle, |\uparrow, \sigma = 2\rangle, |\downarrow, \sigma = 2\rangle$) can be written as

$$H_r(k) = \frac{k^2}{2m} - \mu - \epsilon\sigma_x + \alpha(k_x s_y - k_y s_x)\sigma_z. \quad (\text{S15})$$

The eigenvectors obtained from this model have spin locked to momentum. The resulting spin textures in the normal state reproduce those existing in the literature^{1,2,9}. The model (S15) is also simple enough to solve the Gorkov gap equations.

2.5. Zeeman splitting and pairing potentials

In the presence of a weak magnetic field taken along the x -direction, the Hamiltonian takes the form

$$H_r(k) = \frac{k^2}{2m} - \mu - \epsilon\sigma_x + \alpha(k_x s_y - k_y s_x)\sigma_z - h s_x, \quad (\text{S16})$$

as stated in equation (7) in the main text. We note that we include the magnetic field only as a Zeeman effect, and we ignore orbital effects. The in-plane field breaks the spin degeneracy on each of the two p_r bands, giving rise to four bands with dispersions

$$E(\mathbf{k}) = tk^2 - \mu \pm \sqrt{\epsilon^2 + \alpha^2 k^2 + h^2 \pm 2h\sqrt{\epsilon^2 + \alpha^2 k_y^2}}, \quad (\text{S17})$$

where $t = \frac{1}{2m}$. Clearly, the energy splitting is largest in the k_y direction, which is orthogonal to the magnetic field.

To introduce superconductivity, we consider a Hubbard density-density interaction with two terms, intra-sublayer U , and inter-sublayer, V . The U term can only induce spin singlet pairing, while the V term can induce both singlet and triplet pairings. As we expect U to dominate singlet pairing, we will only consider the spin-triplet component of V . This leaves the simplified interaction,

$$H_{\text{int}} = \int d\mathbf{k} d\mathbf{k}' \left[U \sum_{i,s} c_{i s \mathbf{k}}^\dagger c_{i \bar{s} - \mathbf{k}}^\dagger c_{i \bar{s} - \mathbf{k}'} c_{i s \mathbf{k}'} - V \sum_{i,s} c_{i s \mathbf{k}}^\dagger c_{i \bar{s} - \mathbf{k}}^\dagger c_{i \bar{s} - \mathbf{k}'} c_{i s \mathbf{k}'} \right], \quad (\text{S18})$$

where i and s are sublattice and spin indices, respectively, and bars indicate the opposite value of the index. These interactions can induce four possible pairing potentials $\Delta_1 \propto I$, $\Delta_2 \propto \sigma_z$, $\Delta_3 \propto \sigma_y s_x$ and $\Delta_4 \propto \sigma_y s_y$.

To proceed analytically, we make use of the fact that Cooper pairing occurs primarily at the Fermi surface, and that Fermi surfaces of different bands do not mix. This allows us to treat each Fermi surface separately, projecting onto the electron and hole parts of the Hamiltonian. To be conservative, the Zeeman energy associated with the critical field of β -PdBi₂ is taken to be of the order of the superconducting gap, i.e., ~ 1 meV. Therefore, the magnetic fields relevant to our calculation are much smaller than all parameters of the normal Hamiltonian, which are of the order of 1eV, so we treat the Fermi surfaces as only weakly split by the field. We construct and solve a 2×2 gap equation for each Fermi surface.

The problem thus becomes analytically tractable with the caveat that in the electron-hole basis the pairing potentials have a more complicated \mathbf{k} -dependent structure. The Bogoliubov-de-Gennes Hamiltonian takes the form

$$H_{\text{BdG}}^{(\pm)} = \xi_k^{(\pm)} \tau_z - h \sqrt{\frac{1 + \rho_k^2 \sin^2(\theta)}{1 + \rho_k^2}} s_z \tau_0 + \Delta_{\mathbf{k}} \tau_x, \quad (\text{S19})$$

where $\xi_k^{(\pm)} = t k^2 - \mu \pm \epsilon \sqrt{1 + \rho_k^2}$, $\rho_k = \alpha k/\epsilon$, $\Delta_{\mathbf{k}}$ contains both singlet and triplet pairings. The Pauli matrices τ_x , τ_y and τ_z act on the particle-hole degree of freedom. After projecting each pair potential in the band basis, we found that only pairing states of the same spin around the y -direction, $\sigma_y s_y$, have significant weight. We therefore consider the following two-component order parameter:

$$\Delta = \psi + \eta \sigma_y s_y. \quad (\text{S20})$$

Supplementary references

1. Sakano, M. *et al.* Topologically protected surface states in a centrosymmetric superconductor β -PdBi₂. *Nature Commun.* **6**, 8595 (2015).
2. Iwaya, K. *et al.* Full-gap superconductivity in spin-polarised surface states of topological semimetal β -PdBi₂. *Nature Commun.* **8**, 976 (2017).
3. Shein, I. R. & Ivanovskii, A. L. Electronic band structure and Fermi surface of tetragonal low-temperature superconductor Bi₂Pd as predicted from first principles. *J Supercond Nov Magn* **26**, 1–4 (2013).
4. Tu, X.-H. *et al.* Topological superconductivity in Rashba spin-orbital coupling suppressed monolayer β -Bi₂Pd. *Materials Today Physics* **24**, 100674 (2022).
5. Sancho, M. P. L., Sancho, J. M. L., Sancho, J. M. L. & Rubio, J. Highly convergent schemes for the calculation of bulk and surface Green functions. *J. Phys. F: Met. Phys.* **15**, 851 (1985).
6. Wang, B. T. & Margine, E. R. Evolution of the topologically protected surface states in superconductor β -Bi₂Pd from the three-dimensional to the two-dimensional limit. *J. Phys.: Condens. Matter* **29**, 325501 (2017).
7. Löwdin, P.-O. A Note on the quantum-mechanical perturbation theory. *J. Chem. Phys.* **19**, 1396–1401 (1951).
8. Nakosai, S., Tanaka, Y. & Nagaosa, N. Topological superconductivity in bilayer Rashba system. *Phys. Rev. Lett.* **108**, 147003 (2012).
9. Xu, T. *et al.* Nonhelical spin texture in the normal states of the centrosymmetric superconductor β -PdBi₂. *Phys. Rev. B* **100**, 161109 (2019).
10. Gor'Kov, L. On the energy spectrum of superconductors. *Sov. Phys. JETP* **7**, 158 (1958).